Formation and Break Up of Microscale Liquid Jets

A Thesis Presented to the Academic Faculty

By

Hanif Hunter

In partial fulfillment for the Degree of Masters of Science

George W. Woodruff School of Mechanical Engineering
Georgia Institute of Technology
May 2009

Formation and Break Down of Microscale Liquid Jets

Approved by:

Dr. Ari Glezer
School of Mechanical Engineering
Georgia Institute of Technology

Dr. Marc K. Smith
School of Mechanical Engineering
Georgia Institute of Technology

Dr. Yogendra Joshi
School of Mechanical Engineering
Georgia Institute of Technology

Date Approved:
May 2009

Acknowledgements

The work presented here has been one of the most engaging projects and it pushed my limits especially since it involves a topic in fluid mechanics that is well-known, but seldom covered in undergraduate and graduate courses in addition to the technical difficulties of creating devices to form microscale ($O(10\ \mu m)$) liquid jets. I wish to thank my advisor, Dr. Ari Glezer, who provided very valuable technical guidance through out the execution of the project, allowing it to come this far. The folks in the lab who "put up" with incessant questions and always managed to give an enlightening answer: John Culp, Jelena and Bojan Vukasinovic. Friends in the lab (in no particular order), Rachel Valade, Brett Warta, Ashok Rajendar, George Wu, Philip Abramson, Dan Brzozowski, and Abe Gissen. I would like to thank my father, Maurice Hunter, for giving me the inquisitive mind to discover the truth behind it all and my mother, Ioline Hunter, for giving me the ability to reflect so that I would check the veracity of my words and my knowledge. Good friends, who picked me back up, Nick Menegazo and Pierre Gerardin. The folks who came and left the Gifts, Art, Fun house, especially Celine Lascar, Justyna Weidemeir, and Simone Weber. Folks at Hapkido, who let me open myself up, Master Onsager, Dr. Parlavantzas, Dr. Gay, Dr. Ritchie, Dr. Hall, Dr. Laursen, Ted Skirvin, Melissa Johnson, Philip Dido, Ramaldo Martin, Frank Fearon, and Eposi Litumbe. Dear friend, Miriam Guerrero who put up with me during my undergraduate days at GeorgiaTech.

Table of Contents

List of Tables

List of Figures

List of Symbols and Abbreviations

$\alpha_{th,l}$	Liquid thermal diffusivity.
C	Growth rate constant of a vapor bubble.
$C_{p,l}$	Liquid Specific heat.
Ca	Cavitation number.
D	Jet diameter.
$\Delta\theta$	Dimensionless degree of superheat.
ΔT	Degree superheat.
e	Nozzle orifice eccentricity.
ε/D	Ratio of internal surface roughness of the nozzle and jet diameter.
$h_{f,g}$	Latent heat of vaporization.
L/D	Ratio jet length and jet diameter.
λ/D	Ratio of wavelength and jet diameter.
λ	Wavelength.
ϕ	Ratio of kinetic energies between actual flow and plug flow.
ψ	Splay angle of a branched jet.
ω	Spray angle.
P^*	Pressure ratio.

P_a	Ambient pressure.
P_v	Vapor pressure of the liquid.
r_o	Initial vapor bubble radius.
Re	Reynolds number.
ρ_g	Ambient gas density.
ρ_l	Liquid density.
σ_l	Liquid surface tension.
σ_λ	Standard deviation of the wavelength.
σ_λ/D	Ratio of the standard deviation of the wavelength and jet diameter.
T_a	Ambient temperature.
T_b	Liquid boiling temperature.
V	Jet velocity, evaluated from droplet velocity.
V_r	Radial velocity of droplets.
We_g	Weber number using ambient gas density.
x/D	Ratio of distance from nozzle exit and jet diameter.
$(x/D)_{bu}$	Ratio of break up distance from the nozzle exit and jet diameter.

Summary

The evolution of column instabilities that lead to break up of a microscale (O(10 μm)) liquid jet is studied experimentally using shadowgraph technique. The jet formation is investigated over a range of Reynolds number, Pressure Ratio, and Ohnesorge number which are varied by the driving pressure, observation chamber pressure, and the jet liquid. Over the range of these parameters, the jet experiences different break up mechanisms as a result of different dominant instabilities. The present investigation discusses both break up mechanisms that are similar to the break up of macroscale jets and some new microscale break up phenomena.

Chapter I

Introduction

Micron-scale liquid jets have applications in a number of technical areas including combustion, coating, drug delivery, high resolution printing, microelectronics cooling and particle deposition. The present investigation focuses on the evolution of these jets with specific emphasis on the effects of surface tension, ambient pressure, and jet Reynolds number on their formation and break up. In terms of dimensionless parameters, the present work explores the effects of Reynolds number, Pressure Ratio, and Ohnesorge number on instabilities of microscale [$O(10\ \mu m)$] liquid jets.

The stability of the jet column appears to be influenced by the liquid properties, the flow evolution within the nozzle, and the ambient conditions in the medium into which the jet is injected. Varying these parameters can lead to transitions between several instabilities that radically change the characteristics and evolution of the jet.

This thesis includes five chapters. Chapter 2 reviews earlier works that are relevant to the present jet configurations. Particular attention is paid to five column instabilities. Chapter 3 describes the experimental apparatus and includes details of the fluidic system, optical imaging system, and fabrication and implementation of the micronozzles. Chapter 4 describes the present findings regarding five primary and distinct instabilities of the jet column, including Rayleigh instability, sinuous instability, sinuous instability with jet atomization, jet flashing, and non flashing evaporative jets.

The transitions between these instabilities occur by changing ambient pressure, liquid properties, and jet velocity. Finally, the main conclusions are discussed in Chapter 5.

Chapter II

Literature Review

The work discussed here involves the characterization of the break up and the modes of instability in a microscale [O(10μm)] liquid jet. Understanding the break up mechanisms of microscale liquid jets can benefit a number of applications areas where small scale liquid jets can play a crucial role such as micromachining, ink jet printing, and drug delivery. High precision micromachining using microscale jets would be ideal for micro-fabrication of important surface features that can not be accomplished by chemical etching. Yamaguchi (1997) discussed creating three dimensional microscale structures comparing the advantages of using microscale [O(100 μm)] liquid jets over those of mask-based or focused beam writing methods. Presently, the highest resolution inkjet printers can achieve microscale droplet sizes [O(10 μm)]. Cleary, Singh, Wendorf, and Worsham (2007) developed microinjectors [O(50 μm)] that replace traditional injectors thereby reducing skin irritation associated with drug delivery via injection.

The present experiments identified several instability and break up modes of microscale liquid jets including Rayleigh instability, sinuous instability, sinuous instability with jet atomization, jet flashing, and evaporative jets. Rayleigh instability (Rayleigh, 1879) involves the amplification of small perturbations by surface tension leading to a varicose deformation of a jet column having a uniform velocity profile in a vacuum. Sinuous instability (Rayleigh, 1894) is the inception and growth of asymmetric

disturbances of the jet column manifested by wiggling or by asymmetric surface ripples. This instability is driven both by the flow characteristics within the nozzle and by ambient shear loading on the jet surface. Sinuous instability with atomization occurs when the ambient shear stress on the jet column surface overcomes the liquid surface tension and viscous forces within the jet column leading to amplification of disturbances having wavelengths that are much smaller than the jet diameter. The amplifications of this instability is manifested by the formation of ligaments that peel off the jet column and break up into droplets that are smaller than the jet diameter. Flashing or flash evaporation instability occurs in superheated liquid jets and results in the formation and violent rupture of vapor bubbles that can partially or completely destroy the jet column, producing segmented liquid threads or spray. Evaporation instability results in dramatic changes in the flow and the formation of complex fluidic structures that include hollow cones, films or fanned structures, a bent column, and branched or bifurcated jets. These steady jet structures are maintained by steady and uneven evaporation.

Rayleigh instability of a jet column is driven by surface tension, which amplifies small disturbances and leads to break up into droplets. Savart (1833) studied the break up of a macroscale water jet and estimated the size of the droplets. Lord Rayleigh (1879) theoretically determined that an inviscid liquid jet in vacuum breaks up into droplets if $L/D > 3$ (L is the length of the jet column and D is the jet diameter), a result that was experimentally determined earlier by Plateau (1873). Rayleigh also showed that the characteristic droplet size scales with the wavelength of the disturbance and that the most unstable wavelength is about nine times the jet radius. Tyler (1933) experimentally verified Rayleigh's linear analysis and showed that the most unstable wavelength was

nine times the jet radius for water jets with diameters of 0.352 mm to 0.50 mm and velocities of 0.75 m/s to 2 m/s. Goedde and Yuen (1970) studied capillary instability of water and glycerin-water jets with a diameter range of 2-8 mm focusing on different liquid viscosities and imposed acoustic disturbances using a loudspeaker. They determined that non-linear effects dominate the break up process allowing small wavelengths to grow and form ligaments and satellite droplets. Sterling and Sleicher (1974) improved on the earlier studies of Weber (1931), who analyzed the effects of aerodynamic shear stress on a free jet, and provided a modified version of Weber's theory for jets experiencing Rayleigh instability while under aerodynamic shear stresses. Sterling and Sleicher also suggested that the liquid jet velocity distribution that forms by flow through a nozzle can affect the break up. Jets that evolve with a uniform velocity distribution had longer break up distances than jets that evolve with a parabolic velocity distribution.

Kasyap, Sivakumar, and Raghunandan (2008) also showed how elliptical orifice produced jets that were less stable than circular jets. Their work indicated that the eccentricity of the jet cross-section also plays a role in promoting earlier break up. Kitamura and Takahashi (1978) determined that the nozzle length can affect the break up distance of the Rayleigh instability both in ambient air and in immiscible liquid. They concluded that the nozzle could result in jets with lower exit disturbances and that the growth of these disturbances is affected by the velocity distribution within the nozzle. Mahoney and Sterling (1978) developed a correlation of the break up length as a function of the Weber number, but found that this correlation failed when the ambient pressure was less than atmospheric and the Ohnesorge number was less than 0.28, which was the

experimental range of Fenn and Middleman (1969). Papageorgiou (1995) developed a set of nonlinear evolution equations for long waves ($\lambda/D>1.0$) and demonstrated pinching solutions that predict the appearance and volume of satellite droplets. Furlani (2004) developed a linear theory for a viscous, Newtonian microscale liquid jet with spatially varying surface tension, which at this scale has a strong effect on the evolution of the jet. Moseler and Landman (2000) simulated liquid propane jets evolving from a 6 nm orifice taking into account spatial fluctuations of fluid properties due to evaporation. They studied the effect of wetting and non-wetting nozzle surfaces on the evolution of liquid propane jets formed by oleophobic or oleophilic monolayer coating. Eggers (2002) continued the effort of Moseler and Landman and found that surface tension determines the break up time of nanoscale jets and that vibration disturbance plays a significant role in the final stages of pinching. Shin, Oschwald, Micci, and Yoon (2005) performed a non-equilibrium molecular dynamics simulation on a nanoscale Argon liquid jet; their result indicated that the liquid temperature within the injector was an important factor in determining nanojet behavior.

Sinuous instability is a wiggling or waviness of the jet column resulting from either the influence of nozzle geometry on the flow or from the shear stress in the ambient medium. Rayleigh (1879) observed a wavy formation in the jet column for sufficiently high Reynolds number ($Re>1500$). Smith and Moss (1916) attributed the appearance of the sinuous instability to turbulent flow within the nozzle channel. In an experimental study, Haenlein (1932) determined the transition conditions from Rayleigh to sinuous instability for macroscale castor oil jets. Weber (1931) developed a theory to predict this transition and showed the existence of a maximum in the jet stability curve.

Grant and Middleman (1966) proposed a modified Weber's theory that yielded better predictions for break up distances for liquid jets injected into atmospheric pressure but failed for subatmospheric pressures. McCarthy and Molloy (1973) stressed the effects of nozzle design on the formation of sinuous jets. They showed that various magnitudes of sinuous undulations occurred in jets for the same Reynolds number and Ohnesorge number from different nozzles and they recommended an additional parameter to account for effects of nozzle roughness. Phinney (1975) studied the evolution of turbulent liquid jets (O(1mm)) and noted the negligible affects of varied ambient pressure (93.3, 33.3, and 9.3 kPa) on jet break up; they suggested that the pressure range was not sufficient to affect jet break up. Nagaosa, Matsui, Takuoka, and Sato (1978) and Lasheras and Hopfinger (2000) found that in liquid jets with a surrounding annular air jet, the sinuous undulations and break up depend on the interactions between the two jets. Kerst, Judat, and Schlünder (2000) reported transition to wavy disintegration in liquid jets owing to dissolved gas in the jet liquid. Sallam, Dai, and Faeth (2001) formed sinuous liquid jets and showed that increases in Reynolds and Weber numbers increased the magnitude of the jet column undulations.

It is well-known that liquid jets can be atomized by exploiting nozzle geometries or aerodynamic shear. McCarthy and Molloy (1974) discuss the effect of nozzles on the liquid jet atomization and the affects of aerodynamic form drag on atomizing sinuous jets. Hiroyasu, Shimizu, and Arai (1982) formed jets in high ambient pressure, and found that the spray angle of the jet increases with ambient pressure. Reitz and Bracco (1986) studied the atomization phenomena and proposed a correlation for the spray angle as a function of ambient gas density. Kerst, Judat, and Schlünder (2000) investigated a liquid

jet with dissolved gas and found that ambient pressure played a critical role in the evolution of a spray jet because atomization increases as the jet liquid evaporates in the ambient medium. Arai, Shimizu, and Hiroyasu (1991) showed that a liquid jet is likely to atomize if the flow is separated within the nozzle or if cavitation occurs. Hiroyasu, Arai, and Shimizu (1991) found that fixed cavitation at the entrance of the nozzle channel disrupted the jet so strongly that it appeared as a spray.

The evaporative instabilities of superheated liquid jets are manifested by the formation of bends, hollow-cone, film, and branches in the jet column. Charwat and Russali (1981) formed a 0.1 mm bending water jet by superheating the jet fluid by 40°C. Lin (2003) observed a "bifurcated" jet under audio disturbances that resulted in droplets shedding off the jet column in two primary directions. This bifurcation was an artifact of vibrating the nozzle and not of the jet column separating into branches, which is an entirely new effect not observed previously. The hollow-cone that occurs with the branching was observed by previous investigators. In experiments with superheated liquid jets, Suzuki, Yamamoto, Futagami, and Maeda (1978) formed a hollow cone jet at high superheat (140°C) and jet velocity 14.3 m/s. Kowaleski and Hiller (1993) observed the formation of "wings" and a film like structure when a liquid ether jet was injected into vacuum. They postulated that a delicate balance between jet velocity, evaporation, and structure led to a stable jet.

Flash evaporation or flashing is partial evaporation that liquids undergo with rapid superheating. Flashing jets appear as either column jets with vapor bubbles or as atomized spraying jets which are driven to break up by violent and frequent vapor bubble ruptures. Plesset and Zwick (1953) and Forster and Zuber (1953) studied the phenomena

of flashing, initiating subsequent studies by several investigators. Brown and York (1962) observed flashing jets from nozzles of varying roughness and entrance geometry. They found that geometry played a crucial role in spray formation: the sharp edge geometry with smooth walls yielded a jet column which suddenly broke down into a spray far from the orifice, while rough ($\varepsilon/D = 0.0004$) nozzles broke down into spray at the orifice for the same degree of superheat. Lienhard (1965) reported on the behavior of flashing jets. He specified two regimes, a spray and a column jet broken by vapor bubble explosions that are defined based on the ratio between the velocity generated by "evaporative explosion" and jet velocity. He also showed that the spray angle of the flashing jet depends on the degree of superheat. In a subsequent study, Lienhard and Day (1970) formed superheated water and superheated nitrogen jets and reported the details of formation of and behavior of vapor bubbles and growth time in the jet column. Suzuki, Yamamoto, Futagami, and Maeda (1978) studied superheated water jets, reporting growth rates of vapor bubbles as a function of degree of the superheat. Newnan and Brzustowski (1970) considered liquid carbon dioxide jets which sprayed due to vapor bubble formation and explosion and ultimately evaporated. Chaves, Kowalewski, Kurschat, Meier, and Müller (1988) reported measurements of flashing jet spray angle and determined that the initial angles depend on initial superheat, but increased superheating and interaction with vapor gas and atmosphere results in higher than expected angles for the degree of superheat. Chaves, Knapp, Kubitzek, Obermeier, and Schneider (1995) found that the spray angle became a weak function of injection pressure once the threshold for supercavitation and turbulent flow within the nozzle was reached.

The spray angle of a flashing jet depended more on the interaction between the jet and the ambient atmosphere.

The present work extends earlier investigations of liquid jet instabilities and break up to microscale jets. Rayleigh instability causes break up of microscale liquid jets in the same way a macroscale liquid jet breaks up. It is shown that Pressure Ratio (the ratio of ambient pressure and liquid vapor pressure) and Reynolds number affect the wavelengths that lead to break up of microscale liquid jets by amplifying nonlinear disturbances; this phenomenon also occurs in macroscale jets. These nonlinear disturbances are cavitations, separated flows, and turbulence. Sinuous instabilities appear in the jet column as a result of increases in both ambient pressure and Reynolds number. Sinuous instabilities in the column arise from the flow within the rough nozzle causing cavitation, flow separation, and turbulence and are enhanced by atmospheric shear and turbulence. Sinuous atomization which results from further increases in Pressure Ratio and Reynolds number leads to formation of droplets much smaller than the jet diameter. Evaporating liquid jets injected into a vacuum reveal new behaviors not observed in macroscale jets that include branching, where thermodynamic fluctuation and evaporative cooling fundamentally alter the formation of the liquid jet. Flashing microscale jets are, however, very similar to macroscale flashing liquid jets showing similar behavior when the ambient pressure and Reynolds number change. The present work discusses new behaviors where surface tension forces can affect the formation and break up of a liquid jet of $O(10\mu m)$, which primarily appears in evaporating liquid microscale jets, as well as the modes of break up that microscale and macroscale jets share which are Rayleigh instability, Sinuous instability, Sinuous instability with atomization, and flashing.

Chapter III

Experimental Apparatus

The goal of the present research is to characterize the break up and instability modes of a microscale [O(10 μm)] liquid jet. Section 3.1 discusses the fluidic system (which is designed with a reservoir to assure sufficiently long experiments, at driving pressures up to 6.9 MPa) and the test section. Section 3.2 discusses the nozzle design. Section 3.3 discusses the visualization technique and finally, section 3.4 discusses image and data processing.

3.1 Fluidic System

A schematic diagram of the fluidic system that is used to form liquid jets (propane, butane, hexane, or octane) of varying speeds is shown in Figure 3.1. The maximum driving pressure of the system is 20 MPa and it can hold approximately 40 mL of liquid. The fluidic system has three operational configurations: evacuation for removal of water vapor that may contaminate the working liquid, loading of the working fluid and pressurized dispensing to form a jet. Additionally, the pressure within the test section (in which the jet is formed) can be varied between 11kPa to 401kPa, allowing control of the evolution of the jet.

As mentioned above, the fluidic system is evacuated to remove most of the water vapor and reduce water mixing with the test liquid. To evacuate the system, all valves

are closed, the venturi vacuum pump is started by opening valve, V7, and then vacuum inlet valve, V4, and the three-way valves, V5 and V6, are opened to evacuate the system as shown in Figure 3.1. The pressure transducer, T1, monitors the pressure of reservoir B (Res B). The pressure in Res B is approximately the pressure of the entire fluidic system. The vacuum pressure (measured by T1) is maintained below 5kPa for approximately 30 minutes.

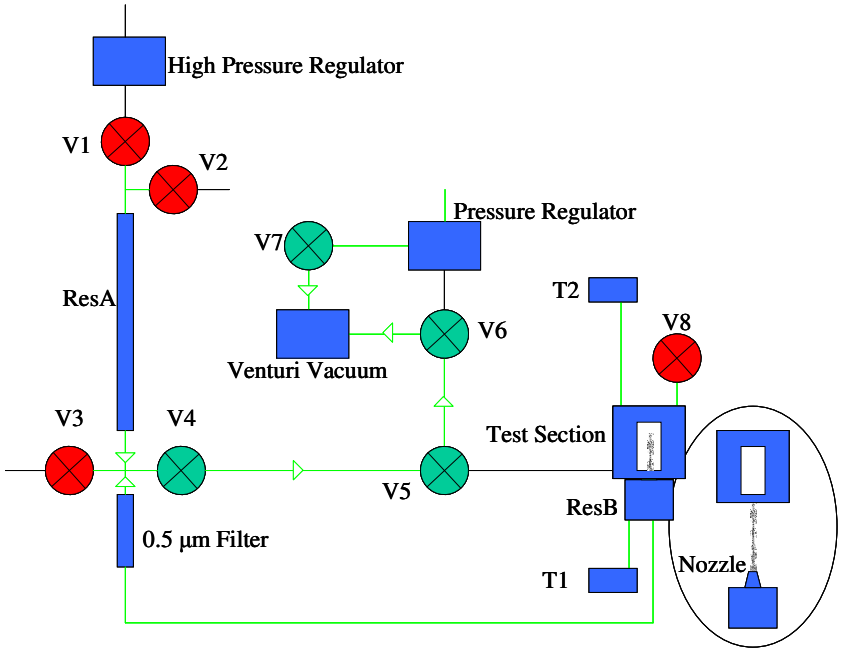

Figure 3.1: Fluidic system schematic in vacuum configuration. Valves in red are closed and in green are open.

After the fluidic system is evacuated, it is filled with the test liquid that forms the liquid jet. Before filling, V4 is closed and the venturi vacuum pump is turned off (by closing V7). The liquid inlet valve, V3, is opened. After approximately 5 minutes, the system relief valve, V2, is opened. V2, which is connected to an open tube, is closed once the test liquid starts flowing from the open end indicating that reservoir A, is filled.

This reservoir is a pipe with an internal diameter of 12.7 mm and a length of 305 mm, holding 38 mL of liquid. The filling configuration is shown in Figure 3.2.

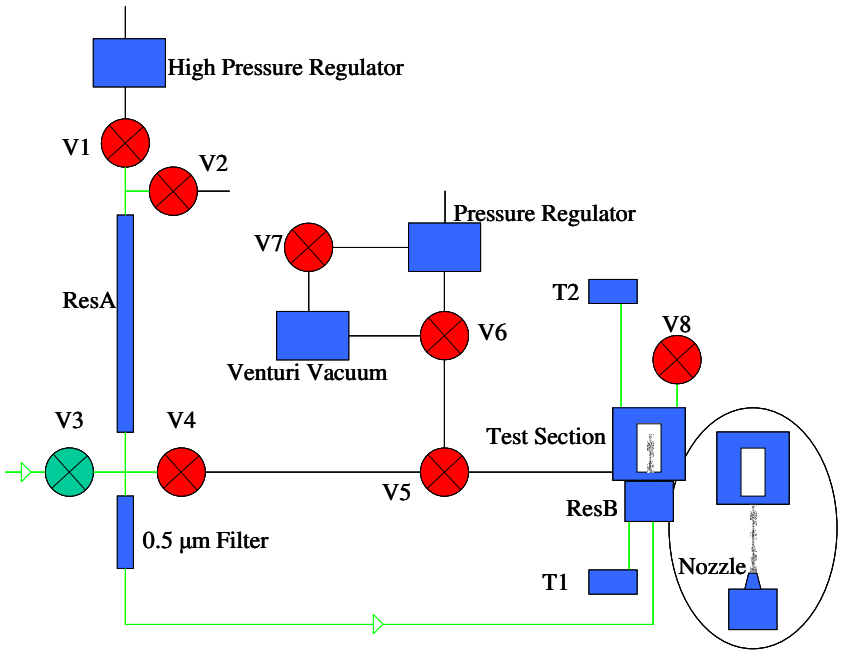

Figure 3.2: Schematic diagram of the fluidic system in the filling configuration. Valves in red are closed and in green are open.

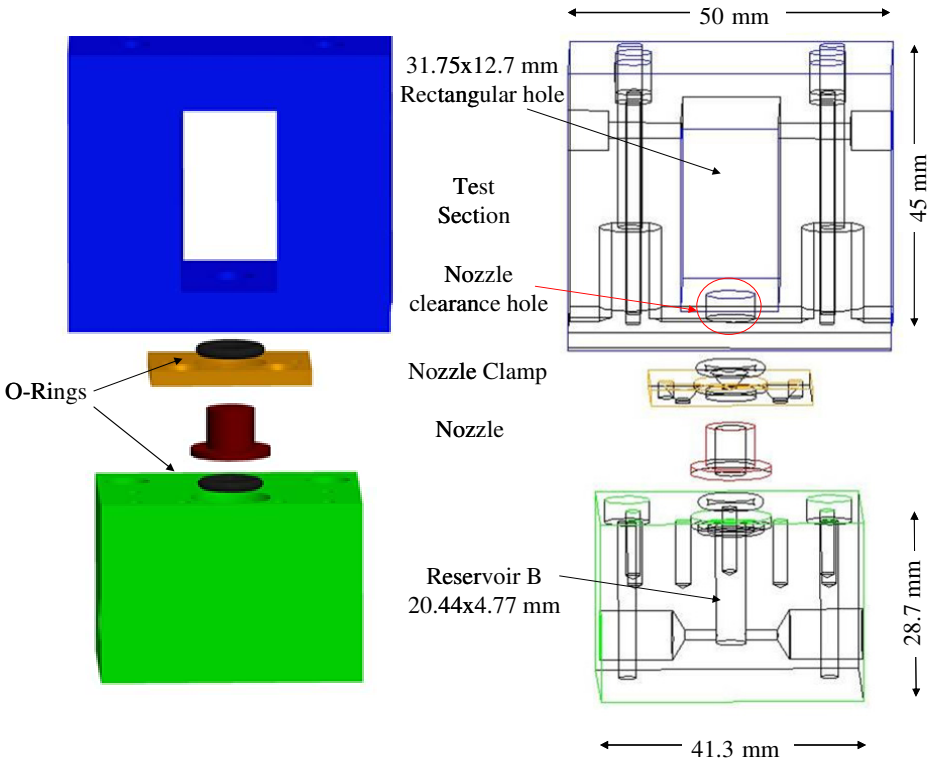

Figure 3.3: Reservoir B, nozzle, and the test section

After V2 is closed, the system is pressurized (0.5 MPa to 4.5 MPa) which provides the driving pressure needed to form liquid jets of varying jet Reynolds number (100-5000). To pressurize, the inlet valve, V1, is opened and the pressure regulator is set to a nominal pressure. The liquid in Res A is driven through a 0.5 μm filter, into reservoir B, and then through a nozzle, to form the jet in the test section. Res B has an internal diameter of 4.77 mm and a height of 20.44 mm (Figure 3.3). The nozzle is seated on an o-ring and is clamped down to this reservoir and the test section is mounted on top of it.

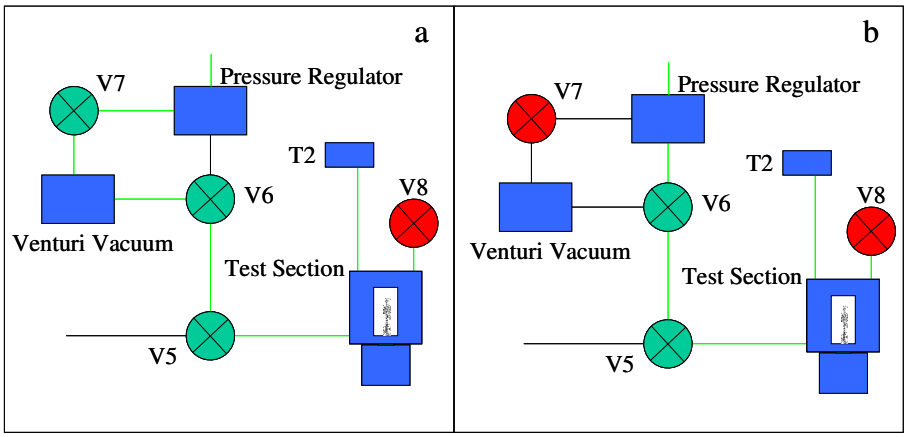

Figure 3.4: The red lines indicate flow paths for the test section for the a) evacuated and b) pressurized configuration. Valves in red are closed and in green are open.

The test section is the enclosure in which the jet forms. It is a rectangular frame with an internal opening that has a cross-section of 12.7 mm by 33 mm and height 31.75 mm. The opening of the test section is sealed on both sides by silica glass plates that are 35 mm high by 25 mm wide and are 5 mm thick. The test section has a clearance hole for the nozzle as shown in Figure 3.3 and the jet can be formed under a range of ambient pressures in order to study the effects of ambient density and evaporation (discussed in section 4.1). The pressure within the test section is monitored by pressure transducer, T2,

and is relieved by valve, V8, which is normally closed during the experiment. To form a vacuum within the test section, V7 is opened and the venturi vacuum pump is operated. The valves V6 and V5 are opened as shown in Figure 3.4a. The venturi vacuum pump is controlled by a pressure regulator to vary the pressure in the test section. To pressurize the test section above atmospheric pressure, V7 is closed while V6 is opened to the pressure regulator (Figure 3.4b) which controls the pressure within the test section.

Once the experiment is completed or the test liquid is exhausted, the system is vented. The valve V1 is closed and V2 and V8 are opened.

3.2 Nozzle Fabrication and Surface Treatment

Several types of nozzles were developed and investigated during the course of this project. The present work has primarily utilized a laser-drilled 10µm stainless steel nozzle.

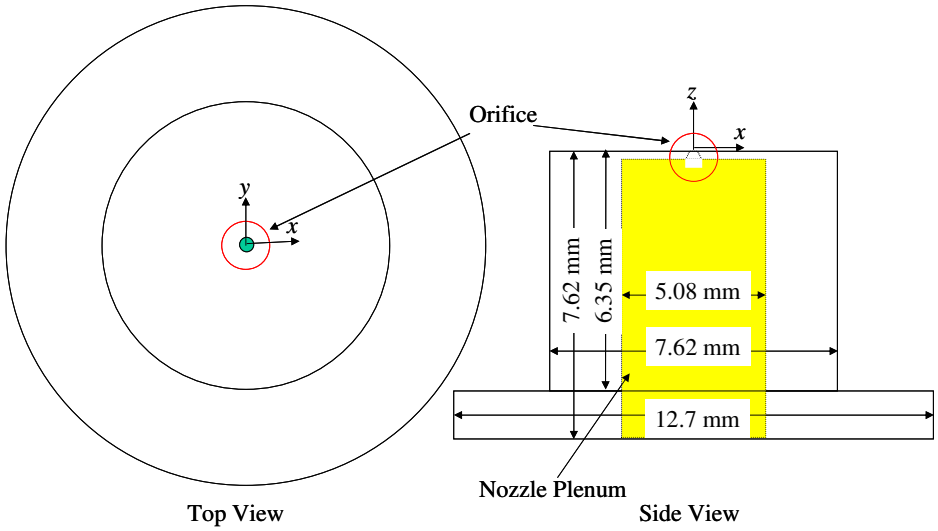

Figure 3.5: Nozzle Schematic, plenum is shown in yellow

The nozzle blank has a top-hat shape with a flange section having a 12.7 mm diameter and 1.27 mm thickness and a cylindrical section having a 7.62 mm diameter and 6.35 mm height (Figure 3.5). The exit plane was polished to create a flat surface to facilitate the imaging of the emerging jet and to reduce surface attraction of the jet liquid. The remaining non-uniformities on the exit plane are on the order of 0.05 µm (the same size of the abrasive powder used in the final polishing slurry). The orifice is a laser-drilled hole through a 1.27 mm thick stainless steel membrane downstream of the 5.08 mm diameter plenum (yellow section in Figure 3.5). The resulting orifice converges from 21 µm to 10 µm and then it diverges to about 12 µm at the exit plane. The precise location of the 10 µm constriction is not exactly known, but according to the

manufacturer it is less than 10D upstream of the orifice exit plane (D = 10 μm). The conduit of the orifice appears to have imperfections on the wall (e.g. the red circle in Figure 3.6) which scale with the wavelength of the laser used to fabricate the orifice (nominally 532 nm).

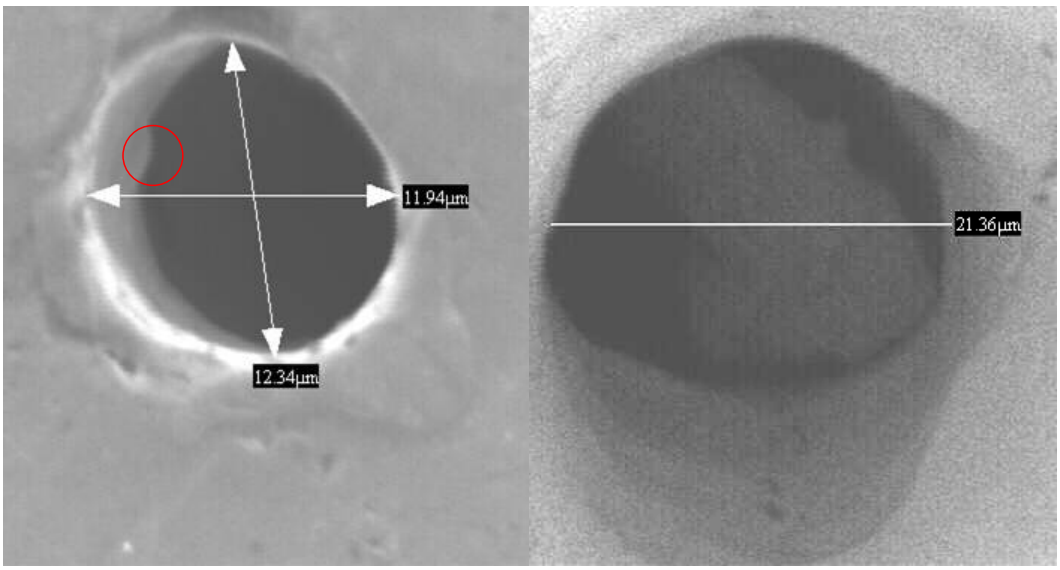

Exit Plane Entrance Plane

Figure 3.6: SEM images of the Exit and Entrance of Orifice

During the initial experiments it became clear that the liquid jets deteriorated rapidly and in many cases stopped flowing as shown in Figure 3.7. It was determined that the cause for this deterioration was the accumulation of contaminants carried by the test liquids in the orifice. The test liquids had a nominal purity of 99.9%. In order to overcome this problem, the nozzle was treated with oleophobic (oil repelling) coating. The contaminants which were typically carried by the test liquid were hydrocarbons. The oleophobic silane used to coat the nozzle was trihydroxysilyl-propane-sulfonic acid (TPSA). This coating is chemically created when the silane bonds to the native oxide

surface of the nozzle. This coating layer is only a few angstroms in thickness, so the change in orifice diameter is insignificant.

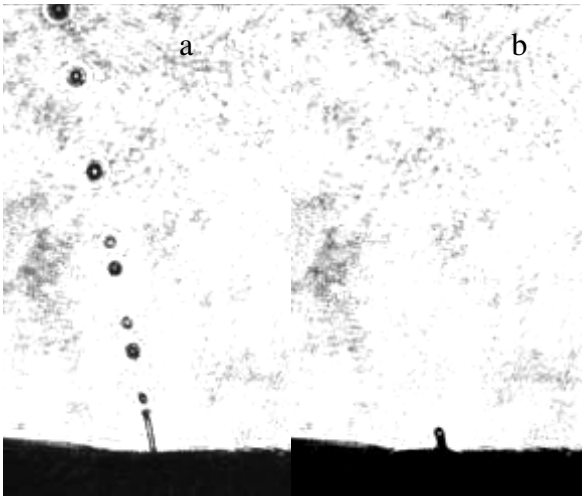

Figure 3.7: Uncoated 10 μm nozzle, driving pressure is 9.6 MPa a) Jetting and b) a deteriorated jet due to partial clogging.

Before treatment, the nozzle was cleaned to remove organic matter and moisture, using detergent, a methanol bath, and drying in a vacuum chamber. The silane was applied using a vapor coating process in an oven that can sustain a vacuum. The nozzle was placed in a container with silane in solution (2% TPSA by molecular weight mixed in methanol). The container was sealed with paraffin paper that allow solvent vapor from the solution to permeate but not the silane vapor. The oven was set to 55º C, evacuated to 10 kPa and the nozzle was treated for 6 hours. After the nozzle was coated, it was placed in an ultrasonic methanol bath to remove any excess silane that may have accumulated on the chemically bonded monolayer and then dried in an evacuated environment.

The coating reduced much of the surface contamination that affected the formation of the jet during the experiment. As mentioned above, untreated nozzles formed jets that deteriorated after a few minutes. With the oleophobic coating, the nozzle

formed a jet for about an hour before any noticeable changes, but still required a 30 minute ultrasonic methanol bath before subsequent experiments. The jets formed by nozzles with oleophobic coating were reasonably repeatable over time with respect to their appearance and break up features.

3.3 Imaging System

As shown in Figure 3.8, the liquid jets were imaged using a shadowgraph technique. To create shadowgrams, the imaging system was composed of a laser, steering optics, microscope objective, and CCD camera. The timing and synchronization of the laser and CCD camera was managed by a laboratory computer using commercial software. Additionally, a mechanical stage was used to shift and tilt the jet in the imaged plane.

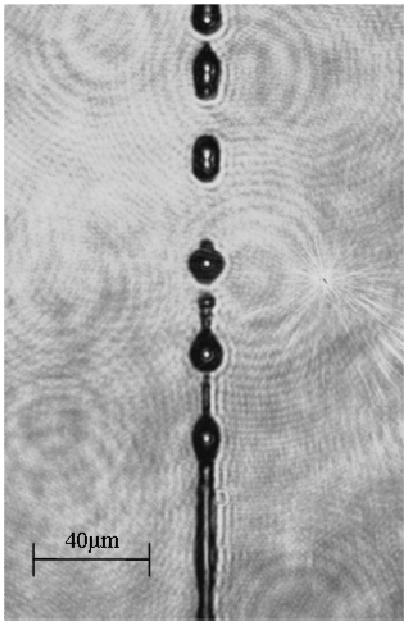

Figure 3.8: Shadowgraph of a 10 μm liquid butane jet.

Shadowgraph technique is an imaging technique that takes advantage of variations in the deflection of light rays from a collimated source due to variation in the gradient of the index of refraction normal to the light ray (Holder, 1963, Settles, 2001). Figure 3.8 shows a shadowgram of a liquid butane jet captured in the present work. The changes in the index of refraction are caused by density gradients and non-uniform liquid interfaces. Light rays from a collimated light source that pass through the cylindrical

cross-section of the jet can be reflected, refracted, or transmitted. The liquid jet effectively acts as a lens that focuses and defocuses incident light causing edges of the jet to attenuate light and centers of droplets and jet column to intensify light as a result of internal reflections (Figure 3.8).

The imaging optics, laser, and CCD camera (Figure 3.9) allow capture of shadowgrams of microjets with speeds up to 100 m/s (using two-frame capture mode with Δt = 1 μs and Δx < 1 mm). The laser is a two-head ND-Yag laser that provides up to 30 mJ of 532 nm light per pulse (pulse width is about 5 ns) with a beam diameter of approximately one centimeter. The laser is operated at maximum Q-Switch delay to reduce the difference in pulse energy between the two heads, which produces a pair of images with consistent intensity levels. The mirrors M1 and M2 in figure 3.9 steer the laser beam through a polarizer, which is used to attenuate the beam. The polarizer also allows for adjustment of beam energy to the CCD camera when the magnification is changed because higher magnification requires higher pulse energy. The beam passes through a 50/50 beam splitter, and one of the beams is stopped by a beam dump. The primary beam passes through the jet test section and is projected on a CCD array by a microscope objective. The microscope objective is comprised of a 5x or 50x element, a zoom collar, and 2x extension tube allowing for a magnification range between 2.28x and 228x at a working distance of 4 cm. The CCD camera is a Lavision Imager Intense, which has 12-bit gray levels and a 1376 by 1040 pixel array and is mounted on a stage that can traverse vertically. The range of the field of view can be varied between 2 mm on the side (2μm per pixel) and 20 μm on the side (20 nm per pixel). The CCD camera

paired with the ND-Yag Laser is capable of capturing two frames down to 0.6 μs apart at a frequency of 2 Hz or capturing single frames at 4 Hz.

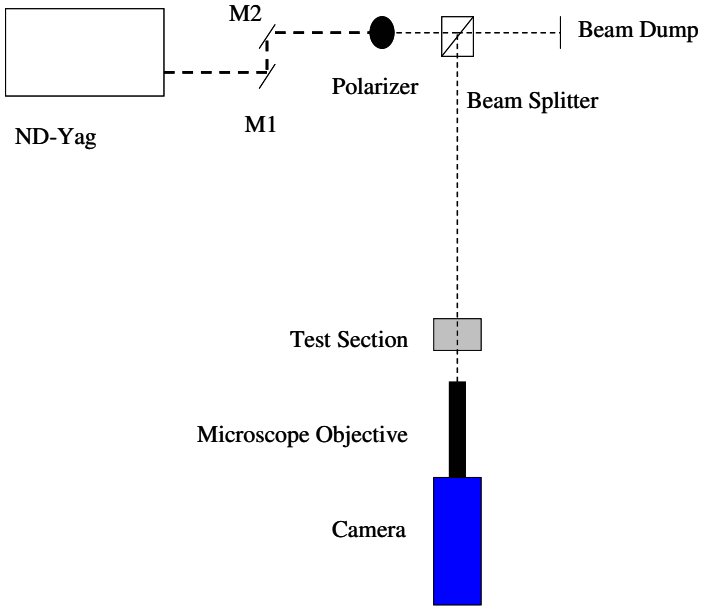

Figure 3.9: Shadowgraph System

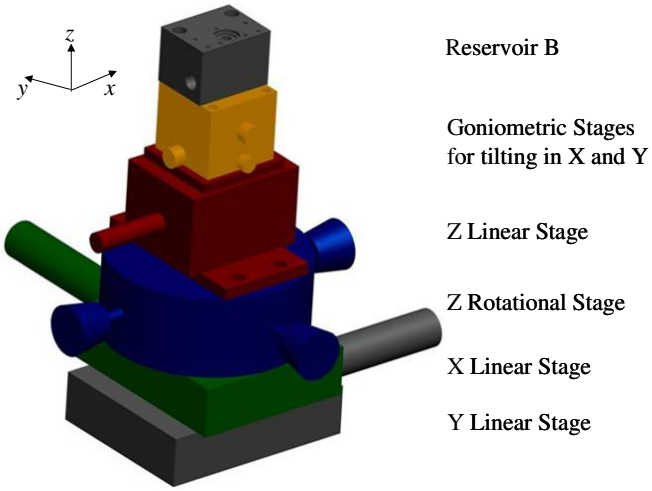

Figure 3.10: 6 axis Stage With Reservoir B

The timing of the laser and CCD camera and storage of the CCD images onto a hard drive are managed using La Vision software (Davis). The imaging system allows

for capture of single and two frames. In a two-frame capture mode, the pairs of images are nominally 1 μs apart, which enable measurement of droplet velocities.

The test section, nozzle, and reservoir B are mounted on a 6 axis stage (Figure 3.10) that can tilt about X and Y axes, rotate about the Z axis and translate in all three coordinates. The X and Y tilting stages are goniometric traverses (on top of the assembly) which enabling tilting of the test section up to 20° with a resolution of 0.01°. Translation along Z (beneath the X and Y goniometric traverse) has 8 mm travel and resolution of 1 μm. The Z rotational stage allows full 360° rotation with resolution of 0.016°. Translation along X and Y has travel of 25 mm displacement and a resolution of 0.05 μm. The entire imaging system, the test section, nozzle and reservoir B are mounted on an optical table with air-operated shock absorbing system.

3.4 Image and Data Processing

Raw images of the jet were obscured by fringes and lack the contrast needed to make the image of the jet stand out. The raw jet images are processed to remove optical aberrations. From these processed images, data such as droplet spacing and speed following the jet break up, break up distance, splay and spray angles are extracted.

3.4.1 Image Processing

Many of the high magnification images require image-processing to remove various aberrations that can obscure the image of the jet column. Fringes create the striations and concentric disks, an example of these fringes is shown in the raw image in Figure 3.11. The striations are caused by sharp-edge diffraction from the nozzle. The concentric disks are caused by diffraction of the collimated light around particulates that contaminate the microscope objective and CCD camera.

The image-processing utilizes a baseline image (without the jet) and is handled in three steps: intensity correction, local shifting, and weighted subtraction. First, intensity correction accounts for variations in laser intensity and results in processed images that have uniform intensities. Second, the raw image is shifted relative to the reference image to account for relative motion between the CCD camera and the test section due to vibrations. Finally, a weighted pixel by pixel subtraction of the baseline image from the raw image removes optical aberrations. The weighted subtraction allows the processed image to retain information of the jet image. Although the processing leaves some banding around the jet column, the details of the jet structure are clearly more visible than in the raw image in Figure 3.15.

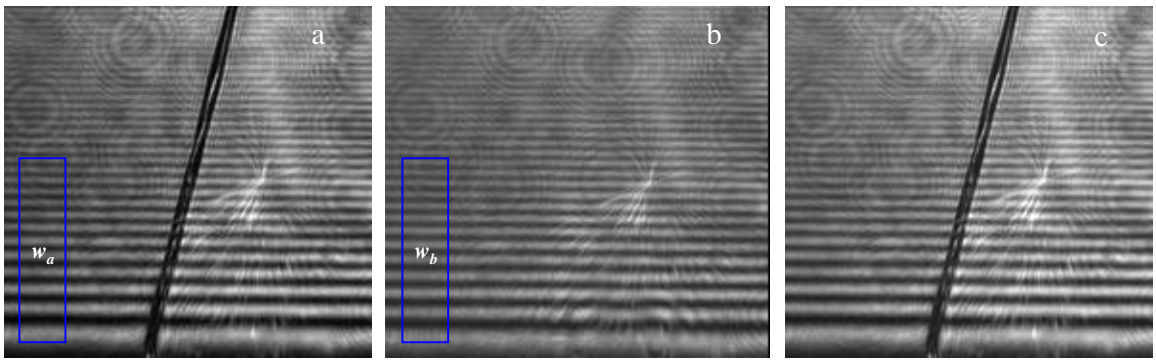

Figure 3.11: Blue windows shown in a) the raw and b) the baseline images are sampled for intensity correction. Image c) is the intensity corrected image.

Intensity correction shifts the average and standard deviation of the intensity of individual pixels of each raw image to match the intensity distribution of the baseline image. As a result, the processed images have a uniform frame to frame intensity. The images are treated as matrices whose entries are the pixel gray levels with a value range of 0-4095. To compute the intensity distributions, corresponding windows w_1 in the raw image in and w_2 in the baseline image (Figure 3.11a and b) are selected. Each window measures of 400x100 pixels. The window, $w_{1,}$ does not include the jet. The pixel intensity in w_1 and w_2 is averaged over the window and the standard deviation is computed. The intensity is corrected by $C_{ij} = \frac{\sigma_b}{\sigma_a}(A_{ij} - \bar{a}) + \bar{b}$, where A_{ij} and B_{ij} are the pixel intensities of the raw and baseline images, $\bar{a}$ and $\bar{b}$ is the average w_a and w_b, σ_a and σ_b are the standard deviation of intensity of w_a and w_b.

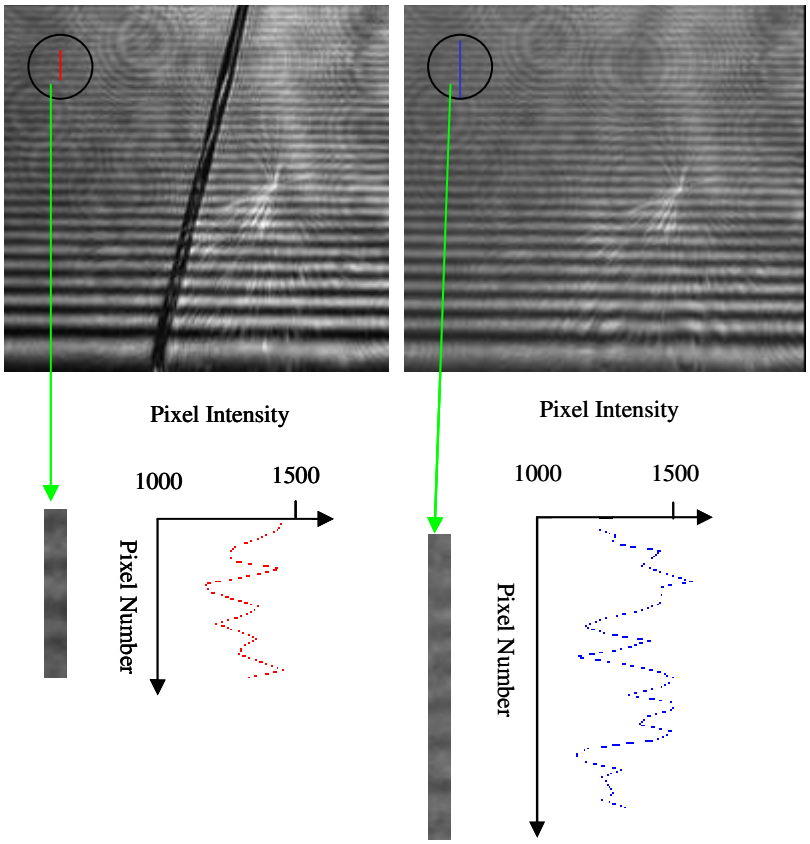

Figure 3.12: Intensity profiles from the raw image (a) and baseline image (b).

Once the raw images are intensity corrected, the relative shift between the raw and baseline image is computed to compensate for small relative motions between the image plane in the test section and the CCD array. It was determined that in the present experiments, the shifts appear to be vertical and therefore the correction shift is determined from two vertical line segments l_1 and l_2 in the raw image and baseline image. The length of the l_1 is 21 pixels and l_2 is 41 pixels (intensity distributions along l_1 and l_2 are shown in Figure 3.12). The intensity profile of l_1 is shifted incrementally as shown in red in Figure 3.13 relative to the intensity profile of l_2. After each incremental shift, the intensity profile of l_1 is subtracted from the intensity profile of l_2 over the length of l_1 and the rms deviation is computed. Figure 3.13 shows the intensity profile of l_1 shifted over

l_2, and the results of the subtraction for shifts of -4, 0, and 4. The shift S is found by minimizing the rms.

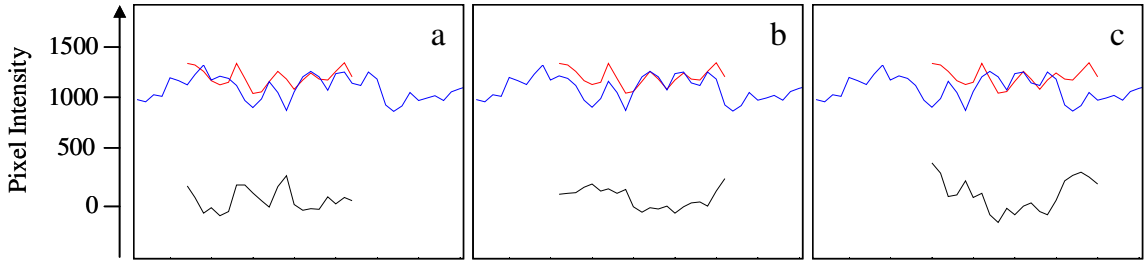

Figure 3.13: Intensity profiles for l_1 (red), l_2 (blue), and their difference for shifts of a) -4, b) 0, c) 4 pixels.

Once the vertical shift of the raw image is computed, the intensity of each pixel of the baseline image is subtracted from the intensity of the corresponding shifted pixel in the raw image. The weight is computed by correlating a rectangular window centered on the shifted pixel in the raw image with a corresponding window in the baseline image. The size of the rectangular window increases from 3x6 to 21x6 as the image is traversed vertically from top to bottom. Figure 3.14 shows how the weight, ρ_{ij}, is computed. A window $\alpha_{i'j}$ from the raw image is centered at pixel (i',j) (which is vertically shifted by S), and a window β_{ij}, from the baseline image is centered at the pixel (i,j). The window $\alpha_{i'j}$ is shifted over β_{ij} and the overlapped elements are multiplied, summed, and then divided by the norms of both $\alpha_{i'j}$ and β_{ij}, which scales ρ_{ij} to values between 0 and 1:

$$\rho_{ij} = \frac{\sum_n \sum_m \left(\alpha_{nm,i'j}\right)\left(\beta_{nm,ij}\right)}{\sqrt{\sum_n \sum_m \left(\alpha_{nm,i'j}\right)} \sqrt{\sum_n \sum_m \left(\beta_{nm,ij}\right)}} \tag{3.1}$$

where $\alpha_{nm,i'j}$ is the intensity of the pixel at (n,m) within $\alpha_{i'j}$, and $\beta_{nm,ij}$ is the intensity of the pixel at (n,m) within β_{ij} (Figure 3.13). The summation occurs over (n,m) the ranges

of (n,m) and (v,w) for which the windows $\alpha_{i'j}$ and β_{ij} overlap. The weighted subtraction of a pixel is computed as $c_{ij} = \left(\alpha_{i'j} - \rho_{ij} \cdot \beta_{ij}\right)$, where c_{ij} is the processed pixel at (i,j). If ρ_{ij} =1, then the windows are identical and full subtraction occurs.

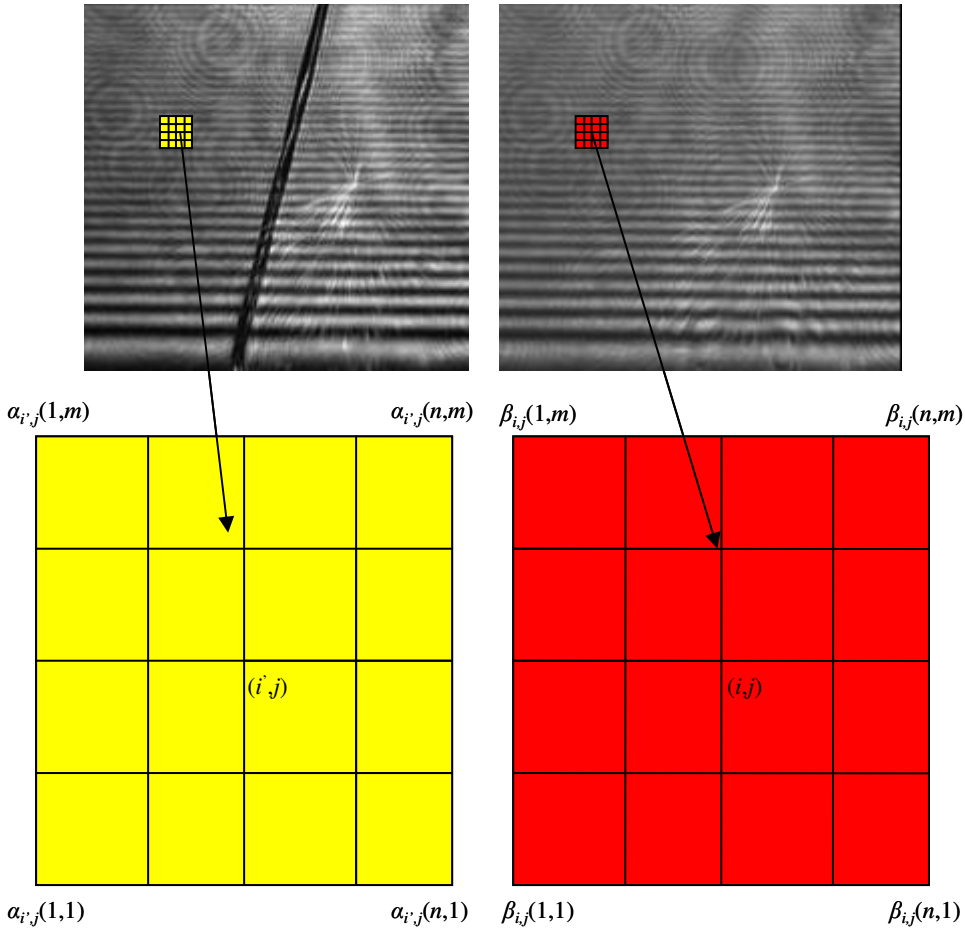

Figure 3.14: Computation of ρ_{ij} from windows taken from the raw image and baseline.

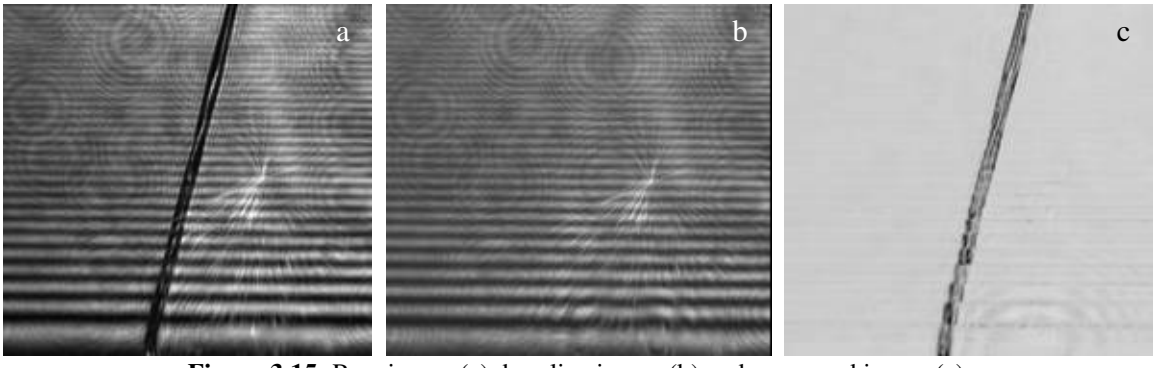

Figure 3.15: Raw image (a), baseline image (b) and processed image (c).

Figure 3.15 shows the final results of the image processing. The raw image shows much of the same fringe patterns as the baseline image and the processed image without very many of the aberrations. There are clearly some imperfections in the processed image such as the banding around the jet column due to the subtraction. It is also important to note that image processing was not always as a result of condensation of liquid on the glass plates that sealed the test section (e.g. images in section 4.4).

3.4.2 Data Processing

Data processing includes measuring various features of the jet such as droplet speeds, break up distances, droplet wavelengths, spray and splay angles in order to relate the effects of Reynolds number and pressure ratio on the those features of the jet column instabilities. Each measurement was made manually using measurement features of the image acquisition software.

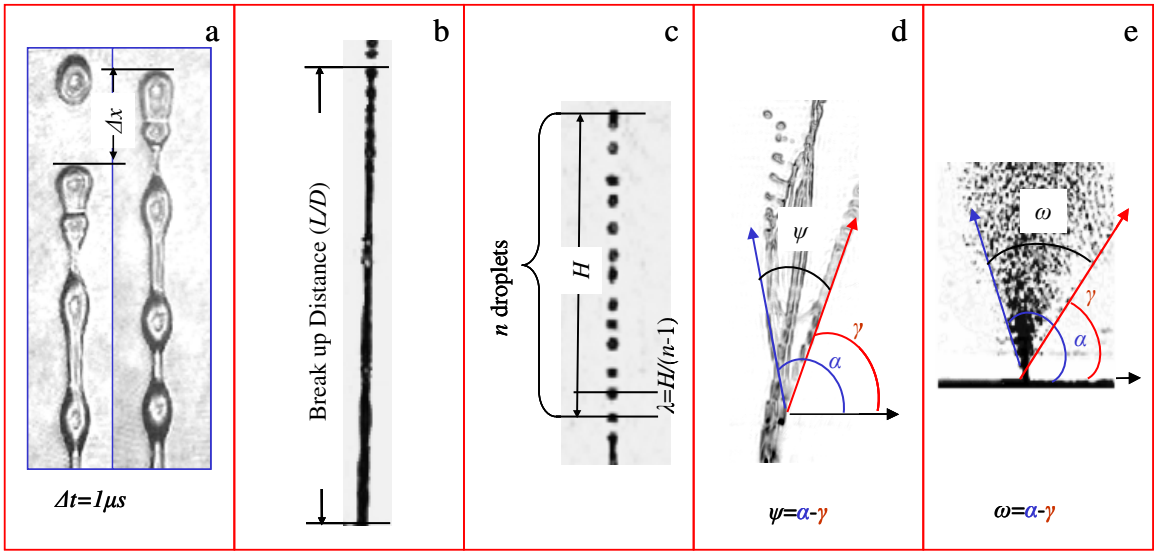

Figure 3.16: Calculations of a) Jet velocity, b) break up distance, c) droplet frequency, d) splay angle, and e) spray angle.

The droplet velocity allows estimates of the jet speed and its Reynolds number. In Figure 3.13a, two images are captured 1μs apart and the relative travel of the droplet shown is from the positions of the tip of the droplet. Care is taken to select droplets that do not deform much and are clearly identifiable.

For discussions of Rayleigh instability (section 4.2) and sinuous instability (section 4.3), assessment of the break up distance and the droplet wavelength are necessary. The break up length indicates the spatial growth of the column instability and the droplet wavelength indicates the most unstable wavelength. The break up distance is computed by finding the distance between the orifice exit and the point of droplet pinch off (Figure 3.13b). The droplet wavelength is computed by measuring the distance between the (approximate) centers of two droplets at the upstream and downstream ends of a train of n droplets and dividing that distance by n-1(Figure 3.13c).

The effect of ambient pressure on a superheated liquid jet, is assessed by the splay and spray angles. The splay angle indicates how ambient pressure affects bifurcated jets (section 4.5.3) and spray angle indicates how ambient pressure affects flashing jets (section 4.6.3). The splay angle is the angle between two jet branches (Figure 3.13d) and the spray angle is the angle of the droplet cone.

Chapter IV

Investigation of Jet Column Instabilities

The present work investigates the evolution of several column instabilities that lead to the break up of a round liquid jet that flows steadily from a 10 μm nozzle, namely, Rayleigh, sinuous, sinuous with atomization, evaporative, and flashing. The evolution of the jet column following the onset of each of these instabilities is radically different and each of these instabilities has unique mechanisms which amplify flow perturbations that cause the jet column to deviate from the smooth cylindrical shape.

- Rayleigh instability is induced by surface tension amplifying a small perturbation and causing a liquid column having a uniform velocity profile in a vacuum to develop surface waves and break up into regularly spaced and uniformly sized droplets. In the present jet, there are several disturbance sources that are amplified by the Rayleigh instability. These disturbances include low amplitude vibrations, interaction with the ambient medium through shear stress, and the adjustment from a solid-liquid to a gas-liquid interface. Once the jet emerges from the nozzle, the disturbances with unstable wavelengths propagate downstream and are amplified by surface tension leading to the formation of necks and swells and culminating in break up of the jet column into droplets.
- Sinuous instability leads to sinusoidal undulations of the jet column, which can result from disturbances within the nozzle (e.g. nozzle geometry and roughness,

transition to turbulence, etc.) and column disturbances that are affected by the ambient conditions (co-axial air flow, cross flow, aerodynamic drag).

- Sinuous instability with atomization is characterized by an undulated jet column that sheds fine droplets having characteristic diameters that is an order of magnitude smaller than the jet diameter.
- Evaporative instabilities arise from surface tension gradients that are caused by evaporation and additional pressure on the jet surface from the expanding vapor phase. The surface tension gradients lead to Marangoni forces on the jet and to bending. The expansion of the vapor phase leads to the development of vapor pockets and branching of the jet column. Branching jets have not been observed on macroscale jets.
- Flashing instability is the appearance of vapor bubbles that rupture and disrupt the jet column. The jet can appear as either a segmented column or atomized spray, depending on the rate of vapor bubble formation. What distinguishes between flashing atomized jets and sinuous instability with atomization is that flashing jets break down from frequent and violent vapor bubble formation and rupture while jets that atomize with sinuous instability do not.

Some of the mechanisms that cause the perturbations which are amplified by the instabilities are discussed in section 4.1, followed by discussions of Rayleigh instability (4.2), sinuous instability (4.3), sinuous instability with atomization (4.4), evaporative instability (4.5), and flashing instability (4.6). These instabilities may be characterized by two primary parameters namely, the jet Reynolds number ($\rho VD/\mu$) and pressure ratio $P^*=P_a/P_v$ (where P_a is the ambient pressure and P_v is the vapor

pressure). Finally, these parameters are used to form a transition map of the instabilities as discussed in section 5.

4.1 Perturbations of a Liquid Jet in Quiescent Air

The perturbations that trigger column instabilities which lead to jet break up can be divided into two groups: perturbations that are induced by the flow within the jet nozzle and perturbations that are induced by interactions with the ambient air. The perturbations from the internal flow through the nozzle can result from sharp corners at the inlet or through the nozzle cross-section (including the orifice), roughness of the internal nozzle surface and the internal geometry of the nozzle and of the orifice at the exit plane. Perturbations that result from the jet flow through a quiescent medium are affected by the ambient density and pressure. In addition, the details of jet break up depend on the liquid properties including surface tension, viscosity, vapor pressure, and density.

4.1.1 Nozzle Entrance

The shape of the nozzle entrance can introduce disturbances that propagate through the nozzle orifice and play a critical role in jet formation. Hiroyasu et al. (1991) discussed the entrance effects on water jets that are formed from nozzles having internal diameters ranging from 0.3 to 3 mm. The authors identified four flow conditions referred to as: super-cavitation, cavitation, wake, and minor disturbances. Super-cavitation results from flow separation within the nozzle. Hiroyasu et al. (1991) reported jets that developed super-cavitation had longer break up distance compared to internal attached flow and broke up from Rayleigh (Section 4.2) or sinuous (Section 4.3) instabilities. Cavitation is associated with the appearance of vapor bubbles within the jet that typically break up the jet into atomized spray when the local pressure is lower than the vapor pressure (Section 4.6). Wakes are disturbances associated with flow separation without

cavitation which can also result in local transition to turbulence. Minor disturbances are flow disturbances that are caused the same geometrical features that can cause wakes, cavitation and super-cavitation, but are not of sufficient amplitude to cause flow separation or cavitation. Hiroyasu et al. (1991) used the Cavitation number, *Ca*,

$$Ca = \frac{P_1 - P_v}{1/2 \rho V_i^2}, \tag{4.1}$$

where P_1 is the pressure upstream of the orifice, P_v is the liquid vapor pressure, ρ is the density of the liquid, and V_i is the jet velocity. The paper reports that in a 3mm round water jet $Ca<0$ indicates the occurrence of super-cavitation, $0<Ca<1$ indicates cavitation, $Ca>1$ indicates the existence of wakes. The cavitation number is used to determine if cavitation drives a jet to break up in flashing instability (Section 4.6).

4.1.2 Nozzle Conduit Geometry

The geometry of the nozzle conduit has a profound effect on the evolution of the jet because it plays a role in establishing the velocity profile of the liquid and the attenuation or amplification of disturbances from the nozzle entrance. For example, Wu et al. (1983) showed that convergent and divergent 0.25-0.35 mm nozzles did not lead to cavitation. McCarthy and Molloy (1974) postulated that the shape of the velocity profile affected the mode of instability in 2.54 mm diameter water jets of different nozzle aspect ratio (*L/D*, length to diameter). Instability modes included Rayleigh instability, sinuous instability and sinuous instability with atomization. These authors proposed a parameter, ϕ, that is the ratio between the kinetic energies of the flow and an equivalent plug flow (having the same average velocity).

Although not suggested by McCarthy, this parameter may account for the effects of different (diverging, converging, and straight) nozzle geometries.

$$\phi = \frac{\int_0^A \{V_z(r)\}^3 \mathrm{d}A}{V^3 A}, \qquad 4.2$$

where V_z is the velocity profile at the exit of the nozzle, A is the orifice cross-sectional area, and V is the average velocity of the jet profile. However, ϕ has limited use since it is difficult to measure the velocity profile.

4.1.3 Nozzle Roughness

Roughness of the inner surfaces of the nozzle can introduce perturbations to the flow that may trigger jet column instabilities [Rayleigh instability (section 4.2), sinuous instability (section 4.3), or sinuous instability with atomization (section 4.4)]. Brown and York (1962) compared the evolution of 0.5 mm water jets through two nozzles, with internal roughness of 0.0004 D and 0.12 D. As described in the paper, while the smoother nozzle produced a jet with a rippled surface, the jet formed by the rougher nozzle was a "ragged stream with ligaments torn from it." Ida, et al. (2002) compared two 10 mm diameter water jets formed from orifices with different internal roughness (0.00063 D and 0.01 D). They showed that the rougher nozzles formed jets with larger surface rippling (one of the main features of sinuous instability) and that these surface ripples grow with jet speed.

4.1.4 Orifice Geometry

The geometry of the exit orifice clearly affects the cross-section of the emerging jet, and can result in disturbances to the jet column that cause earlier break up. The

induced disturbances can grow through the effects of surface tension and surface tension gradients.

Kasyap et al. (2008) discussed how surface tension and non-circular orifice geometries cause instability of the jet column. They reported that water jets produced by an elliptical orifice [O(1mm)] had stronger instability and broke up earlier for $4<We<400$ compared to jets from a circular orifice (We is the Weber number which is discussed in section 4.1.5). The paper reports that for $We<4$ and $We>400$, the break up distance of the elliptical jets coincides with the break up distance of circular jets. However for $We>400$, the elliptical jets are more ruffled in appearance. This indicates that jets formed from a circular orifice are more stable than jets formed from a non-circular orifice because surface tension tends to draw the jet into a circular cross-section; jets that form with non-circular cross-section are subject to perturbations that can hasten their break up.

The Marangoni effect is associated with surface tension gradients that can be introduced by non-uniform evaporation (section 4.1.6). Kowalewski et al. (1993) showed that the Marangoni effect caused a 1 mm ethanol jets to bend due to asymmetric evaporation. They also suggested that once the jet column bends, the lateral circulation, caused by the Marangoni effect, enhances the evaporative cooling preferentially on one side of the jet column, which creates larger surface tension gradient.

It may be important to characterize the eccentricity of the orifice.

$$e = \frac{\sqrt{a^2 - b^2}}{a}, \tag{4.3}$$

where a is the major axis and b is the minor axis of an ellipse (polygons can be approximated by fitting an ellipse or circle that has the same hydraulic diameter).

4.1.5 Aerodynamic Interaction

A jet injected into quiescent gaseous atmosphere has a gas boundary layer on the surface of the column that can result in perturbations from aerodynamic drag, friction loading or transition to turbulence. Most investigators use the Weber number to account for the aerodynamic interaction:

$$We_g = \frac{\rho_g V^2 D}{\sigma_l} \tag{4.4}$$

where ρ_g is the ambient density, V is the jet velocity, D is the jet diameter, and σ_l is the liquid surface tension. This parameter is helpful when assessing the magnitude of aerodynamic interactions relative to the resistive force of surface tension. Sterling and Sleicher (1974) showed that the Weber number plays a role in quantifying the shearing stresses at the surface of a liquid jet. Their theoretical model predicts the experimental break up distances for a variety of liquid jets (water, isopropyl alcohol, and mineral oil) which are formed from nozzles ranging from 1.6 to 2.4 mm in diameter. In the present work the sinuous instability seems to be affected most by *We* as discussed in section 4.3.

4.1.6 Atmospheric Pressure and Degree of Superheat

The atmospheric pressure and the degree of superheat of the liquid can introduce disturbances to the jet column by inducing evaporation or flash vaporization. The degree of superheat relies on the liquid boiling temperature, which depends on the ambient pressure of the medium into which the liquid is injected.

Evaporation decreases jet temperature and can amplify surface tension driven instabilities (e.g. Rayleigh instability), and introduce surface tension driven effects (e.g. Marangoni effect). Also, evaporation can create film-like surfaces. Kowalewski et al.

(1993) discussed the break up distance as a function of ambient pressure on a 0.2 mm ethanol jet injected into a sub-atmospheric environment and jet bending (curving of the jet column caused by Marangoni forces). The authors also described the formation of "wings" created by the "vapor recoil" effect. These "wings," appear to be a film-like surface that peeled from the skin of the jet from what they claimed was additional pressure created by vapor leaving the surface of the jet column.

Flash vaporization involves vapor bubble formation and rupture that destroy the jet column. Lienhard (1966) showed the effects of degree of superheat in his liquid water jets (D=1.25 mm), causing the formation of vapor bubbles which disrupt the jets by forming segmented columns or an atomized spray.

The instabilities caused by evaporation and flash vaporization are affected by the pressure ratio,

$$P^* = \frac{P_a}{P_v}, \tag{4.5}$$

where P_a is the ambient pressure and P_v is the vapor pressure. The normalized degree of superheat is defined as

$$\Delta\theta = \frac{T_a - T_b}{T_b}, \tag{4.6}$$

where T_a is the ambient temperature and T_b is the local boiling temperature. Both parameters are related since liquid properties are evaluated at the ambient pressure and temperature, thus P_v depends on T_a, and T_b depends on P_a so that P^* increases as $\Delta\theta$ decreases.

4.2 Rayleigh Instability

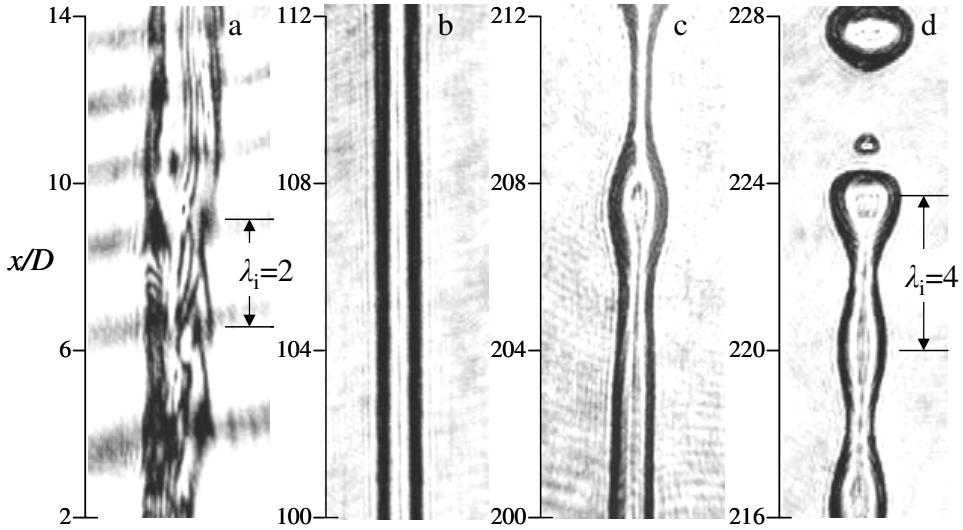

Figure 4.1: Butane Jet Image *Re*=800, P^*=0.25, *x/D*= a) 2, b) 100, c) 200, and d) 216.

Rayleigh instability is a surface tension driven breakdown of a liquid jet column that features the growth of one primary wavelength on the jet column. For *Re*<2000 and P^*>0.1, a microscale liquid butane jet experiences disturbances that distort the cylindrical shape of the column and eventually break up the jet. The evolution and break up of a 10 μm jet column is shown in a sequence of images in Figure 4.1. Each image shows a 10D segment of the jet column at four streamwise positions (*x/D*=2, 100, 200, 216) for *Re*=800, P^*=0.25. The initial disturbance at the exit of the nozzle (Figure 4.1a) is apparently caused by the internal flow within the nozzle. By *x/D*=100, the initial disturbances appear to be dampened and the column becomes cylindrical as shown in Figure 4.1b. While the jet column appears to be undisturbed in Figure 4.1b, it is possible that the unstable wavelength may not have sufficient amplitude to form visible surface waves. Therefore, disturbance sources that include effects of the flow within the nozzle and transition in interface may still affect the jet farther downstream. In addition, the

ambient medium can impart disturbance along the jet column through shear stress. The amplification of these disturbances results in axisymmetric surface waves on the jet column in Figure 4.1c at $x/D \approx 200$. For $x/D > 200$, the surface waves are further amplified by the Rayleigh instability and ultimately the jet breaks up into droplets (Figure 4.1d). Two types of droplets are formed: primary droplets whose diameter is on the order of the jet diameter, and satellite droplets whose diameter is much smaller than the jet diameter. The break up of microscale and macroscale jets appears to be similar. The amplified wavelength for 10 μm liquid jets $\lambda/D=4$ approaches $\lambda/D=4.5$ as predicted by Rayleigh (1894) and the production of satellite droplets is also observed in macroscale jets (Goedde and Yuen, 1970).

4.2.1 Column Evolution

As shown in Figure 4.1a, near the exit plane the jet appears to be disturbed by the flow within the nozzle with a nominal wavelength of $\lambda_i/D=2$. These disturbances may arise from nozzle geometry as discussed in section 4.1. For the entrance flow of the jets shown in Figure 4.1, $Ca=8.9$ may indicate the existence of flow separation at the nozzle entrance creating disturbances that with the roughness of the nozzle ($\varepsilon/D=0.05$) can lead to the appearance of disturbances near the exit plane. Once the jet leaves the orifice, it experiences a strong decrease in shear stress since the shear stress at a liquid-air interface is negligible compared to liquid-solid interface upstream of the nozzle exit. Surface tension reshapes the cross-section of the jet into a circular cross-section and viscosity dampens the disturbances with stable wavelengths induced by the entrance flow, allowing the jet to form an undisturbed circular cross-section (Figure 4.1b). Disturbances that

have unstable wavelengths develop into axisymmetric surface waves that are amplified by surface tension leading to break up of the jet.

4.2.2 Break Up Distance

The jet break up distance, $(x/D)_{bu}$, is defined as the length of the jet column from the orifice to the point of droplet pinch off. The break up distance is discussed here for a 10 μm liquid butane jet for $800<Re<1400$ and $0.1<P^*<1.6$. This distance changes very little over the present range of Re. However, $(x/D)_{bu}$ varies with P^*, ostensibly due to evaporative cooling that reduces the jet liquid temperature and surface tension.

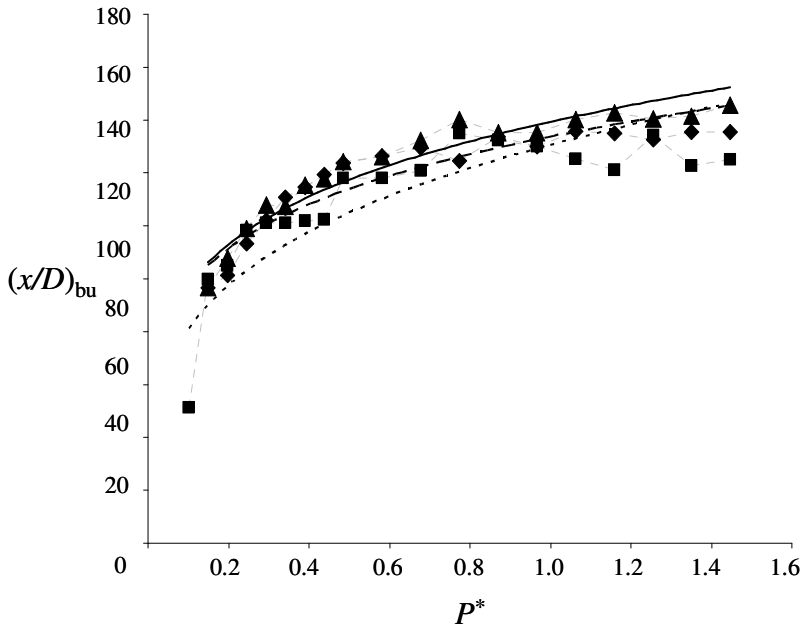

Figure 4.2: Variations of the experimental break up distance with P^* for Re= 800(♦) fitted to curve $154(P^*)^{0.2}$ (--), Re=1100(■) fitted to curve $150(P^*)^{0.27}$ (···), and Re=1400(▲) fitted to curve $159(P^*)^{0.21}$ (—).

Figure 4.2 shows that, for $P^*<0.7$, the break up distance increases with P^*. However, when $P^*>0.7$, the break up distance becomes invariant with P^*. That is, once the ambient pressure approaches the vapor pressure of the jet fluid, $P^* \rightarrow 1$ and evaporation is reduced leading to constant jet temperature and surface tension. As a

result, the break up distance also becomes invariant. Kowalewski et al. (1993) observed similar increases in break up distances of 0.2 mm ethanol jets with increasing ambient pressure (P>20 kPa or P^*>3.4) citing the increase in surface tension with evaporation. The break up distance of Kowalewki's jet did not increase once P>70 kPa or P^*>11.9. It is important to note, the evaporation was primarily driven by vapor diffusion for the range of pressures investigated by Kowalewski. The present work investigates ambient pressures for which, according to Kowaleski, the evaporation is controlled by the gas-kinematic condition. Regardless of the evaporative mechanism, the cooling effects on the jet lead to break up distances that vary with the ambient pressure.

The break up curves shown in Figure 4.2 are fitted to a power laws of P^* that result in R^2>0.7. A power law is chosen because the break up distance is indicative of the spatial growth rate of the unstable wavelengths and decreases with increasing surface tension, which is inversely proportional to P^*.

4.2.3 Liquid Droplet Formation and Behavior

The breakup of the jet column as a result of Rayleigh instability leads to the formation of droplets (Figure 4.3). As noted above, there are two primary droplet scales namely, primary droplets that scale with jet diameter and satellite droplets that have a nominal diameter of 0.1 D. The formation of primary droplets from a jet column initiates as a swell of liquid (Figure 4.3a), that grows into a bead connected by a thin ligament of fluid (Figure 4.3b). The internal pressure is greater in the ligaments than in the swell of the jet column due to the ligaments having smaller radii of curvature (Goedde and Yuen, 1969). Therefore, the surface tension force, which increases with decreasing diameter, induces an adverse axial pressure gradient that leads to fluid flow from the thin ligaments

of the jet into the thicker swells. Eventually the droplet pinches when the ligament is too thin to sustain any mechanical loading (Figure 4.4). The ligaments that the primary droplets pinch off from may also pinch off to form satellite droplets or recede into the jet column. If the ligament recedes, its tip becomes rounded and then is absorbed into the upstream swell (Figure 4.5). After pinching off, the droplets travel downstream at a velocity of 10 m/s and undergo vibrational modes (Figures 4.4 and 4.5), which are eventually dampened by viscous forces and the droplet become spherical, by surface tension forces.

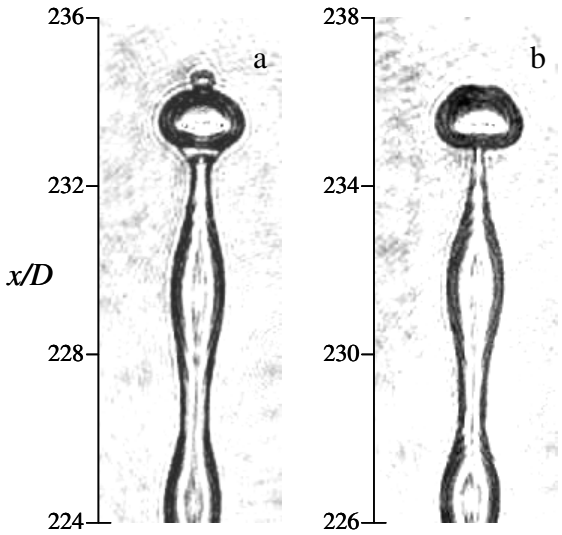

Figure 4.3: Formation of droplets at *Re*=800 and P^*=0.25. Images a) and b) are 1 μs apart

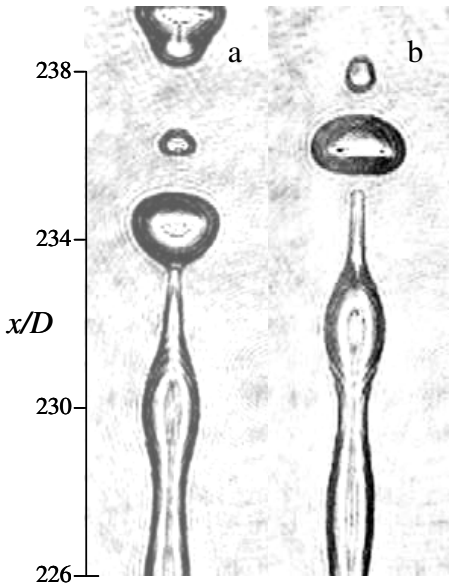

Figure 4.4: Detachment of a droplet at *Re*=800 and P^*=0.25. Images a) and b) are 1 μs apart.

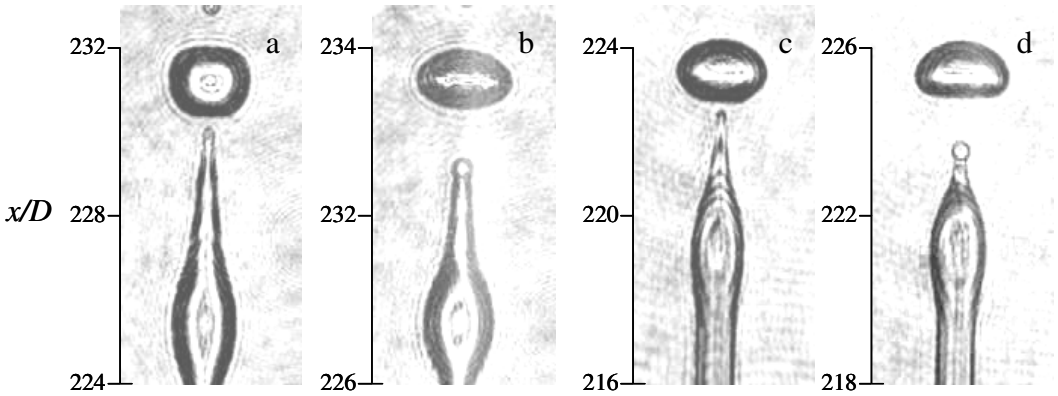

Figure 4.5: Recession of pinched ligament at *Re*=800 and P^*=0.25. Images a) and b) are 1 μs apart and images c) and d) are 1 μs apart.

The ligaments that pinch from the jet column develop into satellite droplets as shown in Figure 4.6. These ligaments do not recede back into the jet column, but instead develop an internal swell as a result of the necking at both ends and pinch under surface tension forces as shown in the red circles in Figure 4.6a and b. Once detached, these ligaments contract further and form a spherical droplet (Figure 4.6c and d). Some of these satellite droplets continue to travel at about 10 m/s while other, slower satellite droplets merge with the faster moving, larger primary droplets (Figure 4.7). The lower

velocity of some satellite droplets are a result of earlier pinch off and recession of the ligament at the downstream end than in the upstream end, allowing surface tension to accelerate more mass in the direction opposing the flow, and thereby reducing the overall momentum. Figure 4.6c and d shows a satellite droplet traveling about 8 m/s. This phenomenon is discussed by Goedde and Yuen (1970) who investigated the formation of acoustically driven satellite droplets from 4 mm water jets.

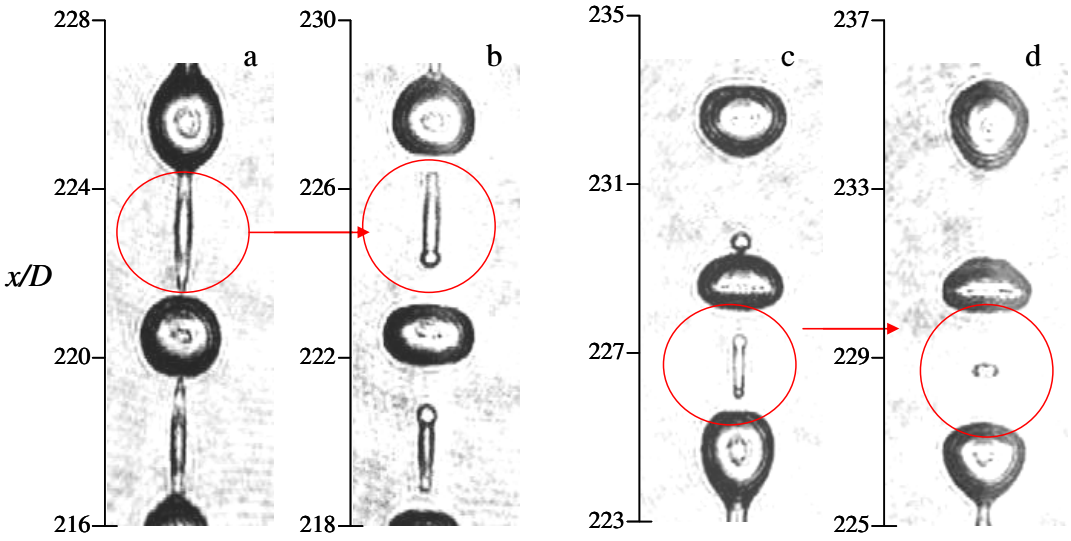

Figure 4.6: Formation of satellite droplets at *Re*=800 and P^*=0.25. Images a) and b) are 1 μs apart and images c) and d) are 1 μs apart.

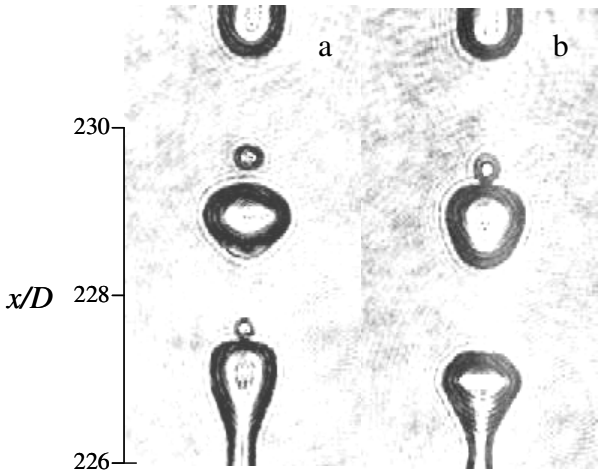

Figure 4.7: Absorption of satellite droplets at *Re*=800 and P^*=0.25. Images a) and b) are 1 μs apart.

As shown by Pimbley (1975), the break up of the jet into primary and satellite droplets are the result of the Rayleigh instability, but the formation of satellite droplets indicates a non-linear break up. The primary droplets are the result of a linear break up, in which the necked region progressively thins until pinching occurs in the center of the necked region and not at the extremities of connecting ligaments as predicted by Rayleigh (1879). The appearances of satellite droplets, which evolve from ligaments that pinch at their extremities, indicate the instabilities at wavelengths smaller than what was predicted by Rayleigh's linear stability analysis, which does not predict the formation of satellite droplets.

4.2.4 Liquid Droplet Wavelength

The droplet wavelength is an estimate of the wavelengths of the disturbance that are amplified and break up the jet. The wavelengths that are amplified are known to vary with liquid properties and jet velocity and as such can be affected by P^* and Re. This was noted by Weber (1931), who derived a relationship which showed that a decrease in velocity and increases in viscosity lead to an increase in the characteristic unstable wavelength.

The parameter, P^* affects the thermodynamic properties of liquid butane of the jet column, and is studied to determine the effects on the average wavelength of break up. Average wavelength is the average distance between approximately 40 pairs of droplets for one value of Re and P^*. Octane and hexane jets are not formed under sufficient ambient pressures for evaporative cooling to occur. The average wavelength for a butane jet had no clear relationship with P^* (Figure 4.8). The fit created for each case (holding Re constant) show no consistent feature (e.g. similar slope) and have R^2 values of 0.6 or

less. The error is computed in order to compare with the scatter of the average wavelengths. The error of measuring the length of a train of droplets (described in section 3.4.2) is nominally 10 pixels over a minimum length of 100 pixels and 5 droplets, which is 10/100/5 or 2% error. For temperature fluctuations of 1°C in the ambient temperature, surface tension varies by 1%, viscosity by 2% and density by 0.3%. Summing the errors gives about 5.3% error in the wavelength, which is at most 0.2D. This indicates that the error is fairly small and does not account for the scatter therefore leading to the conclusion that the present range of P^* has minimal or no affect on the average unstable wavelength. Therefore, the wavelengths are averaged over P^* and studied for dependence on *Re*.

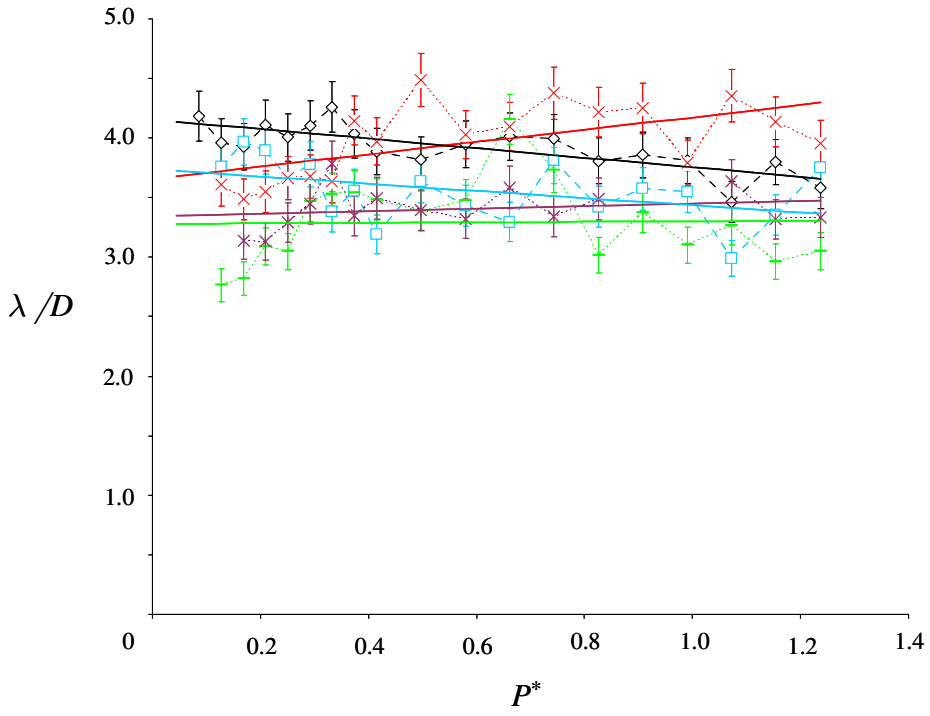

Figure 4.8: Variations of droplet wavelength (λ/D) with P^* for *Re*=800 (◊) fitted to -4(P^*)+41.5 (—), *Re*=1120 (□) fitted to -3(P^*)+37.3 (—), *Re*=1430 (×)fitted to 5.2(P^*)+36.5 (—), *Re*=1790 (—)fitted to 0.2(P^*)+32.8 (—), *Re*=2030(×)fitted to 1.1(P^*)+33.4 (—) for butane.

Table 4.1: Pressure Ratio-averaged droplet wavelength

Re	λ/D averaged over P^*	σ_λ/D	% of Data within $2\sigma_\lambda$
Butane			
800	3.9	0.19	0.95
1120	3.6	0.26	0.94
1430	4.0	0.31	1.00
1790	3.3	0.35	0.94
2030	3.4	0.18	0.93
2300	3.5	0.38	1.00
2430	3.2	0.24	1.00
2710	3.1	0.28	1.00
2950	3.0	0.21	1.00
Hexane			
550	4.4	0.22	0.95
970	3.7	0.27	1.00
1330	3.3	0.41	1.00
1440	2.7	0.17	1.00
1680	2.9	0.22	0.95
1800	3.2	0.23	1.00
2060	3.1	0.27	1.00
2170	3.3	0.24	0.95
2300	3.1	0.35	0.95
Octane			
360	4.3	0.20	0.95
540	3.9	0.23	0.95
710	3.9	0.16	0.95
820	3.8	0.17	0.95
930	3.6	0.23	0.94
950	3.5	0.26	0.94
1030	3.4	0.13	1.00
1070	3.8	0.20	0.95
1200	3.4	0.43	1.00

Tables 4.1 shows the *Re*, average wavelengths averaged over P^*, standard deviation, and the percent of data within $2\sigma_\lambda$. Wavelengths were averaged over 0.1<

P^*<1.2 for butane, over 0.6< P^*<15.1 for hexane, and over 6.0< P^*<162.8 for octane. Table 4.1 shows that 95% or more of the data lay within $2\sigma_\lambda$ of the average over P^*. As such, for a value of *Re*, the wavelength averaged over P^* is used to show how the wavelength is affected by *Re* and is simply referred to as the average wavelength.

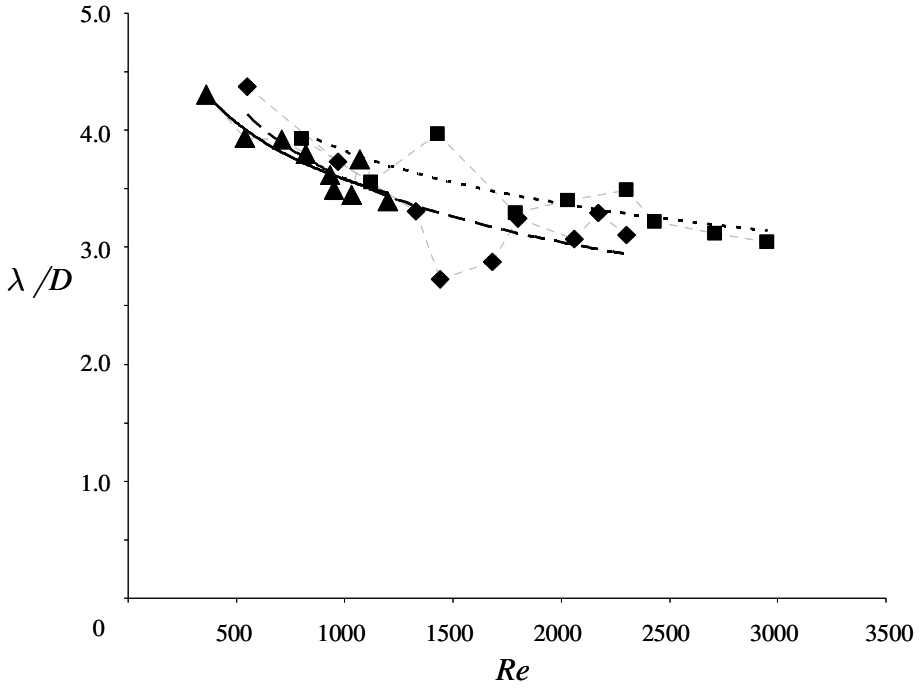

Figure 4.9: Variations of droplet wavelength with *Re* averaged over P^* for a butane jet (■) fitted to curve $134Re^{-0.18}$(···), hexane jet (♦) fitted to $186Re^{-0.24}$(--), and octane jet (▲) fitted to $126Re^{-0.18}$(—).

Figure 4.8 shows how the average wavelength (λ/D) varies with *Re* based on the data in Tables 4.1. These data indicate that the average wavelength decreases as *Re* increases. Specifically, for *Re*<500, $\lambda/D\approx4.5$, in agreement with the prediction of Rayleigh (1879). Weber (1931) analytically showed that the unstable wavelength grew with the exponential of the jet velocity squared. Efforts to fit a log relationship to the present data yields R^2>0.3 and a power law is chosen instead to fit the data, giving R^2>0.6. The average wavelength, λ/D, appears to decrease by $Re^{-0.18}$ for butane and octane and by $Re^{-0.24}$ for hexane as shown in Figure 4.9. The difference in power is not

clearly understood, but butane may behave like octane as a result of evaporative cooling. It is conjectured that the decrease in wavelength with *Re* is associated with the increased effect of the disturbances that are induced by the nozzle. The diminishing rate of the decrease indicates transition from Rayleigh break up to sinuous instability (Chapter 4.2).

4.3 Sinuous Instability and Break up

Sinuous instability is characterized by undulation in the jet column and the appearance of a ruffled surface throughout the entire length of the column. Early investigators of jet break up phenomena observed these column instabilities (Rayleigh, 1879 and Smith and Moss, 1916). The instability tends to be driven by disturbed flow from the nozzle and aerodynamic interaction with the jet column, as discussed in section 4.1. Separated flow at the nozzle entrance may still be present since Ca=15 (Hiroyasu et al., 1991). As noted in Section 3.3, the present nozzle has a conduit surface roughness, ε/D=0.005 and Re>1700, which implies the flow within the conduit is approaching the transition range.

4.3.1 Transition to and Evolution of Sinuous Instability

As noted above, the transition of a liquid jet from Rayleigh instability to sinuous instability is manifested by the appearance of wavy undulations on the jet column. Figure 4.10 is a compilation of high-resolution images of five jets each comprised of a composite of four views (height of 30D) that are stitched together. Each jet in Figure 4.10 is chosen to illustrate the differences between Rayleigh and sinuous instabilities and the evolution of sinuous instability with Re and P^*. Figures 4.10a-d exhibit sinuous instability, while in Figure 4.10e the jet column undergoes Rayleigh instability, which is characterized by its smooth jet column. In Figures 4.10a and b, where Re=1790, the jets appear to be similarly disturbed and seem unaffected by the increase in P^*. In Figure 4.10a and c, where P^*=0.29, the jet appears to be slightly more disturbed for higher Re. However, in Figure 4.10b and d, where P^*=1.45, the jet column is significantly disturbed

for higher *Re*. It appears that the dominant parameter that amplifies the sinuous instability is *Re*.

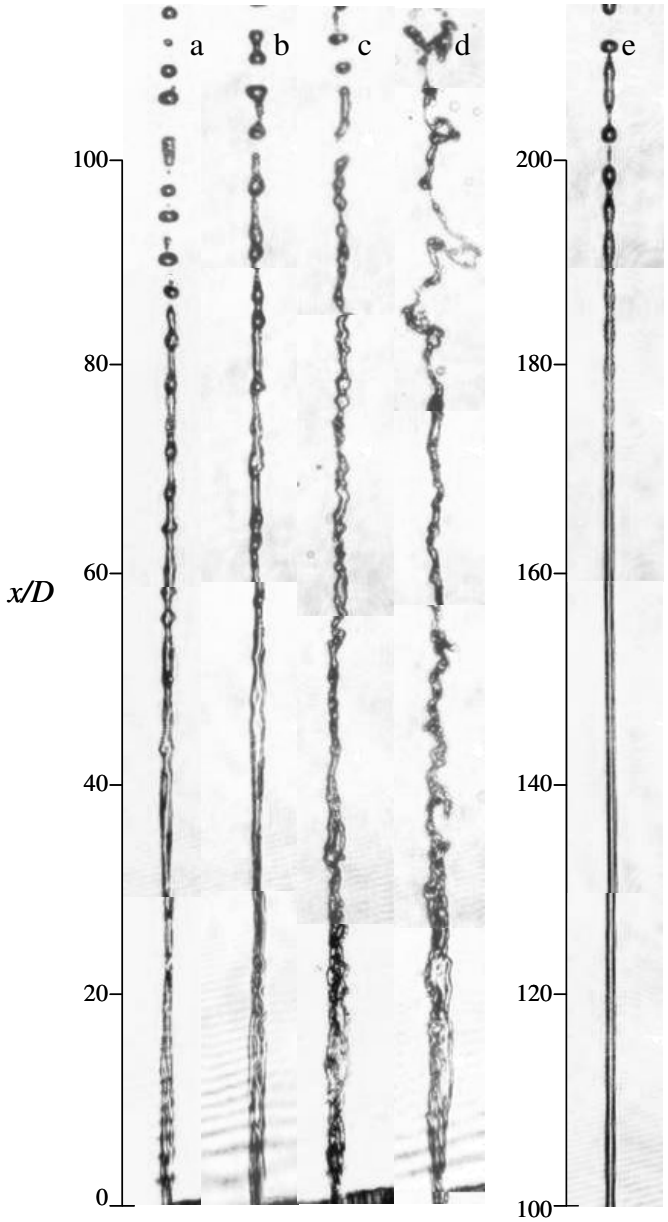

Figure 4.10: Butane Jet column a) *Re*=1790 P^*=0.29 We_g=1.7, b) *Re*=1790 P^*=1.45 We_g=8.5, c) *Re*=2950 P^*=0.29 We_g=4.6, d) *Re*=2950 P^*=1.45 We_g=23, and e) *Re*=800 P^*=0.29 We_g=0.5

The most dominant perturbation may be identified by the Weber number for each case in Figure 4.10. According to the Weber numbers of the jets in Figure 4.10b (We_g=8.5) and c (We_g=4.6), there should be more ambient interactions for the jet in

Figure 4.10b than in 4.10c, but the jet in Figure 4.10c appears more disturbed. This may indicate that the instability is primarily affected by perturbations from the nozzle and less so by ambient interactions. However, ambient interaction does amplify disturbances in the jet column as shown by Figure 4.10c and d, where the jet in Figure 4.10d has a column that is more distorted downstream from the nozzle than the jet in Figure 4.10c. Increases in both Re and P^* increases both the aerodynamic drag and the likelihood of turbulent air boundary layer. This behavior is in agreement with Kerst et al. (2000), who defined a transition to wavy instability that depends on Re and P^*. This transition to wavy instability occurs sooner as both Re and P^* increases. This behavior is apparent in the jet in Figure 4.10d (Re=2950 and P^*=1.49).

4.3.2 Break up Distance

For a given P^* the break up distance $(x/D)_{bu}$ decreases when the jet transitions from Rayleigh to sinuous instability. For example, for P^*=1.0, $(x/D)_{bu}$ for Rayleigh and sinuous instability are 140 and 80, respectively. It appears that the disturbances that originate from nozzle geometry (sections 4.1.1 to 4.1.3) are not attenuated for Re>2000 and propagate downstream. Grant and Middleman (1966) discussed the rapid decrease in the jet break up distance with Re and indicated that the decrease in break up distance was accompanied with jet transition from Rayleigh instability to sinuous instability (Figure 4.11). They noted the jet developed "severe waves" but still was destroyed by symmetrical disturbances (it is assumed that they were referring to Rayleigh instability). This is what appears to happen in Figure 4.10a-c, while in 4.10d, the jet break up into strands of liquid.

For a given Re, the break up distance $(x/D)_{bu}$ increases with P^* as shown in Figure 4.10. The break up distance for jets with sinuous instability appears to become constant for $P^*>0.4$. The break up distance appears to decrease for $P^*>1.3$, but there is insufficient data to conclude the behavior. For the break up curves of jets with sinuous instability, a power law is once again chosen and $(x/D)_{bu}$ is fitted to $90(P^*)^{0.13}$ with $R^2=0.94$.

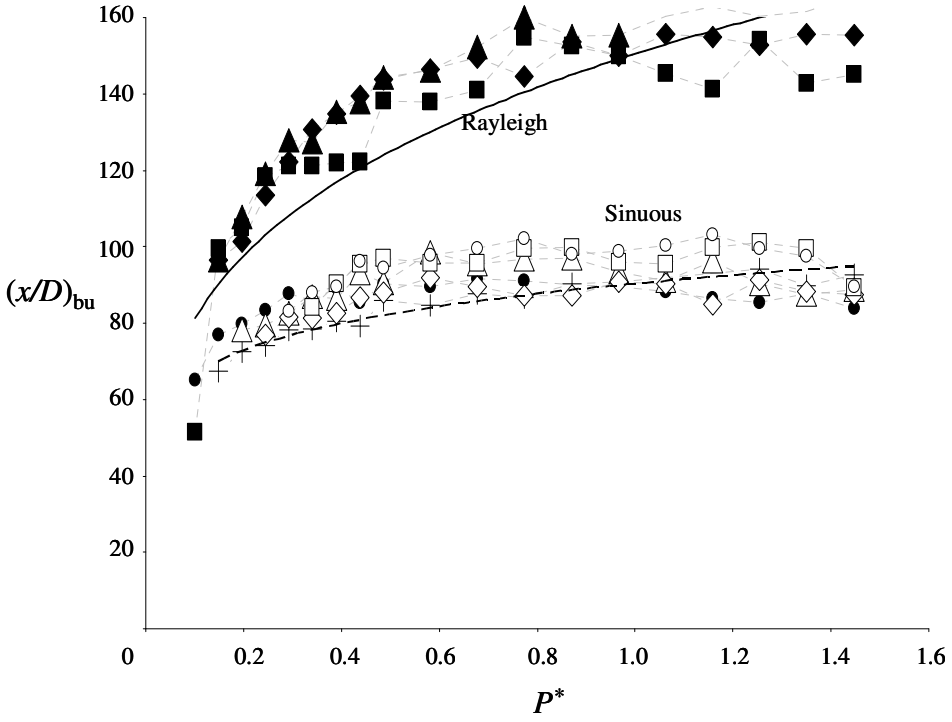

Figure 4.11: Variation of Break up distance over dimensionless pressure: jets with Rayleigh instability *Re*= 800(♦), 1100(■), 1400 (▲) fitted to curve $x/D=154(P^*)^{0.2}$ (—), jets with sinuous instability *Re*=1800(•), 2030(+), 2300(Δ), 2430(◊), 2710(□), and 2950(○) fitted to curve $x/D=90(P^*)^{0.13}$ (--).

4.3.3 Droplet Evolution

Droplet formation as a result of the sinuous instability is characterized by a broad distribution of irregularly shaped droplets. While the droplets in Figure 4.12a (*Re*=1790) are reasonably spherical, in Figure 4.12b (*Re*=2950), the jet column transforms to strands that are connected by ligaments. For *Re*=1790 (Figure 4.12a), the break up is still induced by surface tension and the effect of the sinuous instability is weak, while for

Re=2950 (Figure4.12b) the sinuous instability mechanically breaks strands of liquid off the jet column before individual droplets can pinch off as discussed by Grant and Middleman (1966).

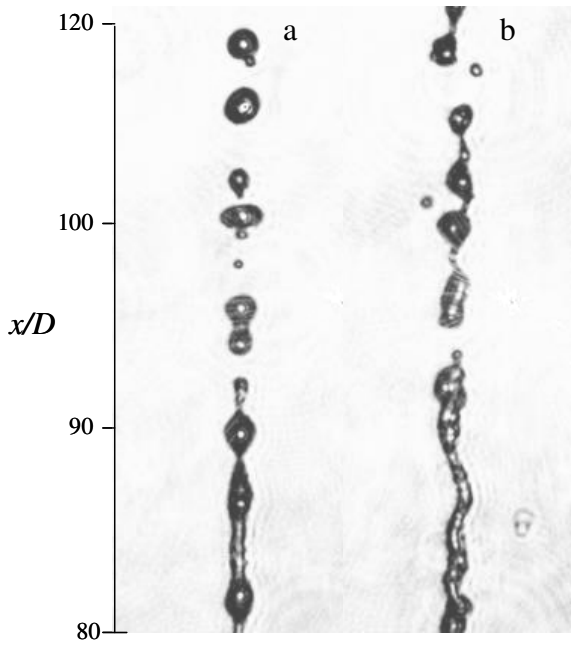

Figure 4.12: Sinuous instability break up for P^*=0.29 at *Re*= a) 1790 and b) 2950

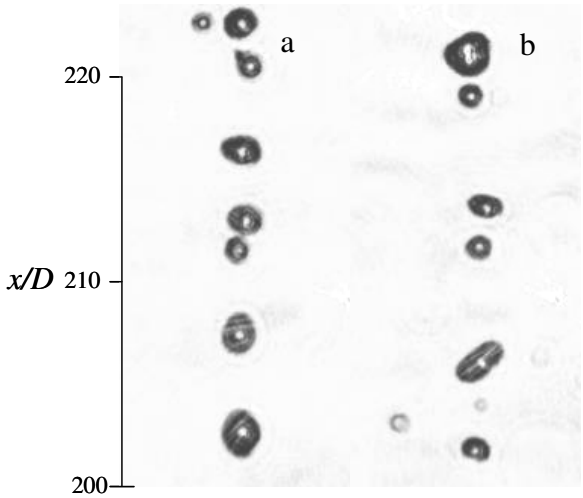

Figure 4.13: Jet droplets at P^*=0.29 *Re*=a) 1790 and b) 2950

The same jets are also shown farther downstream (from *x/D*=200) in Figure 4.12. In this streamwise region, the train of droplets in Figure 4.13a (*Re*=1790) and 4.13b

(Re=2950) are similar. The characteristic wavelength appears to increase from an average wavelength of 2.9 in Figure 4.13a to 3.3 in Figure 4.13b (using the method described in section 3.4.2) which is within two standard deviations of the mean, 3.0 ± 0.4, as shown in Table 4.1 for *Re*=2950. Closer study of Figure 4.13 indicates a greater spread in wavelengths (computed by measuring the distance from the centers of two droplets) 1.5D to 5D, indicating amplification of multiple disturbances other than those with the wavelength of 4.5D predicted by Rayleigh.

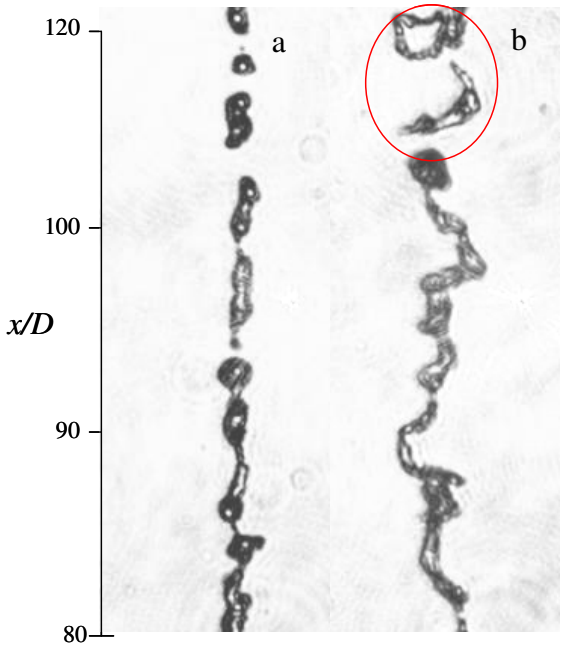

Figure 4.14: Jet column at *Re*=2950 P^*=a) 0.29 and b) 1.45, irregularly shaped droplets in red circle.

Increasing P^* and *Re* affects droplet shape and evolution, by amplifying undulations on the jet column. The sinuous instability affect on the jet is so profound that the jet column in Figure 4.14b (P^*=1.45 and *Re*=2950) appears a highly irregular, sinusoidal liquid thread in comparison to Figure 4.14a (P^*=0.29 and *Re*=2950). The result is the production of highly irregular shaped droplets shown in the red oval in Figure 4.14b.

4.4 Sinuous Atomization

Sinuous atomization is characterized as the break up of a jet by sinuous instability into droplets that propagate in both the streamwise and radial directions. Figure 4.15a and b shows the effect of P^* on a butane jet undergoing sinuous instability. An increase in P^* from 1.45 (Figure 4.15a) to 1.93 (Figure 4.15b) leads to sinuous atomization as shown by the cluster of droplets (in the red oval).

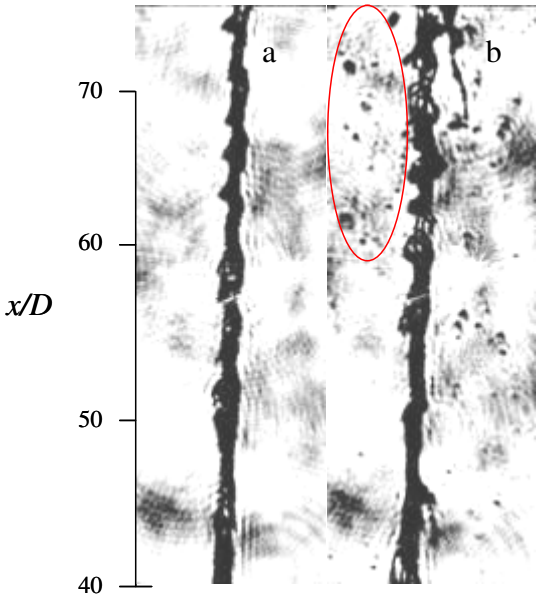

Figure 4.15: Evolution of sinuous atomization with increasing P^* in a butane jet (Re=2950), P^*=1.45(a) and P^*=1.93(b).

Kerst et al. (2000) cited two main factors that caused a methyl myristate jet (2.09 mm diameter) to break up from sinuous instability into atomized spray when injected into an ambient CO_2 gas at a pressure of 8 MPa. First, the affects of the ambient gas increases with pressure because the density of CO_2 increases from about 20 kg/m^3 at 1 MPa to 200 kg/m^3 at 8 MPa. Second, the ambient gas dissolves into the jet liquid, which changes the jet liquid properties. For example the surface tension of methyl myristate decreases from 25 x10^{-3} N/m at 1 MPa to 5x10^{-3} N/m at 8 MPa. However, it is conjectured that since the

present jet fluid is a light hydrocarbon, the partial pressure of butane increases with the ambient pressure which increases the density of the ambient medium. The computed ambient density at P^*=1.93 (401 kPa) without evaporation is 4.77 kg/m^3, but taking into account the partial pressure of evaporated butane from the jet, the ambient density becomes 14.62 kg/m^3. By comparison, the ambient gas at P^*=1.45 (301 kPa) is 4.13 kg/m^3 without and 10.82 kg/m^3 with evaporation. Hiroyasu et al. (1982) reported increased production of fine droplets with ambient pressure (0.1 MPa to 70MPa) in 0.3 mm water jets injected into nitrogen medium. The paper shows photographic evidence of jets experiencing increased instability by increasing the ambient pressure from 1 MPa to 2 MPa. The authors claimed that the ambient density increases with the perturbing force of the ambient medium on the jet, as is discussed in 4.1.5.

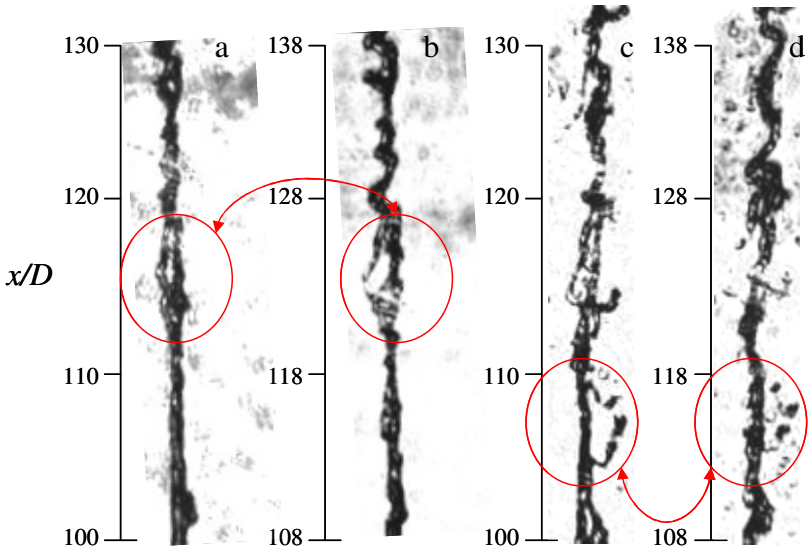

Figure 4.16: Butane jet at *Re*=2950 and P^*=1.93. Images a) and b) are 1µs apart and show the formation of a liquid thread. Images c) and d) are 1µs apart and show the break up of the thread into distinct droplets.

The break up of the ligaments that form as a result of sinuous instability is illustrated in Figures 4.16(a,b) and (c,d). These figures show pairs of images taken 1 µs apart. Figures 4.16 (a, b) show the formation of a ligament (in the red oval). The break

up of a similar ligament is shown in Figure 4.16c and d as a result of surface tension forces. The formation of the droplets appears to be similar to the droplets discussed by Hoyt and Taylor (1977), who produced water jets from a converging 6.35 mm nozzle. They attributed the formation of ligaments to hair pin vortices, but there is no evidence that this is the same phenomenon in the present work.

4.5 Evaporative Instabilities

As mentioned above, evaporative instability is driven primarily by evaporation from the surface of the liquid butane jet column. In particular, the effects of an eccentric nozzle along with evaporation from the jet column surface introduce surface tension gradients that can lead to jet bending and the formation of film structures. Additionally, the effect of reduced ambient pressure (Section 4.1.6) can lead to the formation of vapor pockets and branching jets. Typically, these effects are observed for $Re<3500$ and $P^*<0.15$, although several investigators (e.g. Kowalewski et al. 1993) observed evaporative instabilities up to $P^*=1$.

4.5.1 Jet Bending

Bending of the jet column can occur due to the Marangoni effect. In the present work, the bending effect is the result of non-axisymmetric evaporation from the jet column that that is coupled with the nozzle eccentricity ($e=0.25$). The evaporative butane jets bent in two configurations. For $Re=1380$ and $P^*=0.075$ the jet column undergoes a stable and repeatable bending. However it is shown that for $Re=500$ and $P^*=0.13$, the jets develops a vapor pocket and a bend in the jet column.

Bending owing to asymmetric evaporation is shown in Figure 4.17. Figure 4.17a ($P^*=0.08$) shows the jet issuing vertically but has a disturbed surface due to the orifice eccentricity as discussed in section 4.2.1. Once pressure is reduced, the evaporation of liquid from the surface of the asymmetric jet column causes surface tension gradient which bends the jet (Figure 4.17b). The radial force needed to bend the jet as shown in Figure 4.17b is estimated from integral methods to be about 22 μN, which precludes

"vapor recoil" as a bending mechanism, since the difference in pressure that is needed across the jet column to cause such a bend is estimated to be 146 kPa. The repeatable and steady bend is most likely the result of a Marangoni effect driven by asymmetric evaporation from the jet column. Steady bending jets were also observed by Charwat et al. (1980) who investigated a 0.1 mm superheated water jet. They demonstrated steady bends for superheats of 35-40˚C at ambient pressures of 17 kPa (which corresponds to a range of P^*=0.0018-0.0016, based on the computed vapor pressure of water at the mentioned superheats). These authors determined that the bends depend on the superheat (and by extension P^* as discussed in 4.1.6) and a result of asymmetric evaporation but gave no indication of the location of the bend. In an attempt to rationalize the asymmetry of the evaporation from the jet surface, Charwat theorized that some disturbance originating from the nozzle exit (e.g. an asymmetric nozzle exit) causes initial asymmetry in the evaporation and bending of the jet. They further claimed that the curvature with the velocity profile "led to circulation" that sustains the asymmetric evaporation and curvature, for which there exists no experimental evidence.

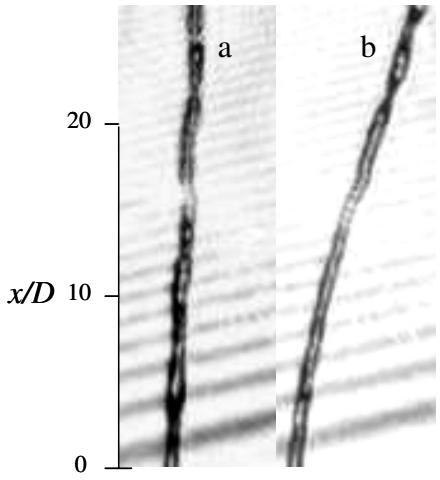

Figure 4.17: Bending of a butane jet under reduced ambient pressure, *Re*= 1380 P^*=0.08(a) and 0.075(b).

Vapor pocket formation and jet bending occur unsteadily and simultaneously for evaporating butane jets at Re=500 and P^*=0.13. The vapor pocket appears intermittently and disturbs the column imposing a void within the jet column as shown in Figure 4.18. The images are separated by approximately 300 ms and the duration of the vapor pocket is less than 600 ms (determined by the frequency of image capture). In the absence of a vapor pocket, the jet issues vertically (Figure 4.18a), but when a pocket appears, the jet bends. The vapor pocket can form as a result of the "vapor recoil" effect (Section 4.1.6 and Kowalewski, 1993) and the jet bends as a result of surface tension gradients as a result of evaporation from non-circular jet cross-section. It may also be argued that the formation of the vapor pocket can introduce a disturbance to the jet column and result in a bend at the vapor pocket as shown in Figure 4.18b. Figure 4.18b shows a thickened part of the jet column (red oval), which is the initiation of a vapor pocket accompanied by bending of the jet column. In addition, jet column downstream appears ruffled and seems to be disturbed by the appearance of the vapor pocket. (blue ovals in Figure 4.18b and c).

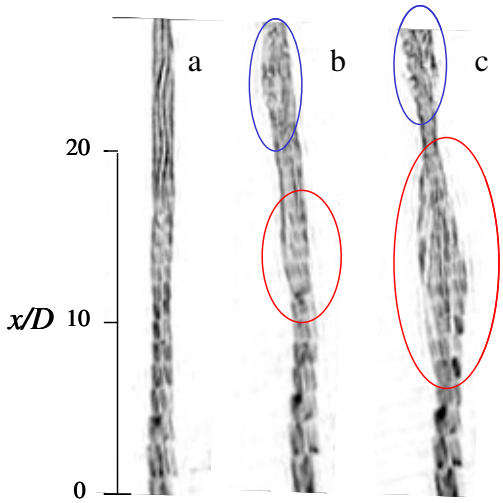

Figure 4.18 Butane jet experiencing bending and vapor pocket formation, Re= 500 and P^*=0.13. Red ovals show the location of vapor pocket formation and blue ovals indicate ruffles in the jet.

4.5.2 Hollow-Cone Formation and Branching

Many investigators have reported jet with hollow structures at a critical superheat and ambient pressure, but the present work reports an additional oscillatory behavior when a jet forms a hollow-cone structure along with branches. Hollow-cone formation and branching occurs when the vapor pocket grows and opens and separates the jet column into two or more branches as shown in Figure 4.19a. The hollow-cone structure is indicated in the red ovals in Figures 4.19c-f. The structure is characterized by the formation of a conical void in the jet column that is open at its downstream exit to ambient medium and partially encased by a liquid film (blue ovals in Figure 4.19) that in the present work are attached to branches. Kowalewski et al. (1993) proposed that the inner core of their evaporative 0.2 mm ethanol liquid jet was warmer than the surface. This hypothesis can explain the formation of the hollow-cone and branches because it implies that the inner surface of the hollow-cone may experience greater evaporation. Presumably, the fluid from the jet core flows to the inner surfaces of the film and leads to greater evaporation rate and "vapor recoil" on the inner surfaces of the films which sustains the hollow-cone structure. The liquid film that makes up the hollow-cone structure is cooler than the upstream core which leads to surface tension gradients that creates Marangoni flow into the film and therefore sustains the film. The formation of branches in the hollow-cone structure may be the result of the geometry of the nozzle along with the "vapor recoil" effect causing the jet to branch in a particular configuration as it does in the present work.

For P^*=0.065 and Re=500, the vapor pocket oscillates between a trapped vapor pocket to a hollow-cone state as shown in the sequence of images in Figure 4.19. This

form of state oscillation has not been reported by earlier investigators. Since the oscillations occur in a timescale that can not be resolved by the present imaging system, the sequence of images in Figure 4.19 is ordered from the collected data to show how the vapor pocket can transition to a hollow-cone. In the closed state, the jet branches encapsulate a vapor pocket as shown in Figure 4.19a. In Figure 4.19c to f, the jet vapor pocket opens into a hollow-cone structure creating individual branches connected by liquid film. It is noted that some branches appear to break up as a result of Rayleigh instability. This branch break up has not been reported by earlier investigators. Finally, the hollow-cone begins to close again in Figure 4.19g.

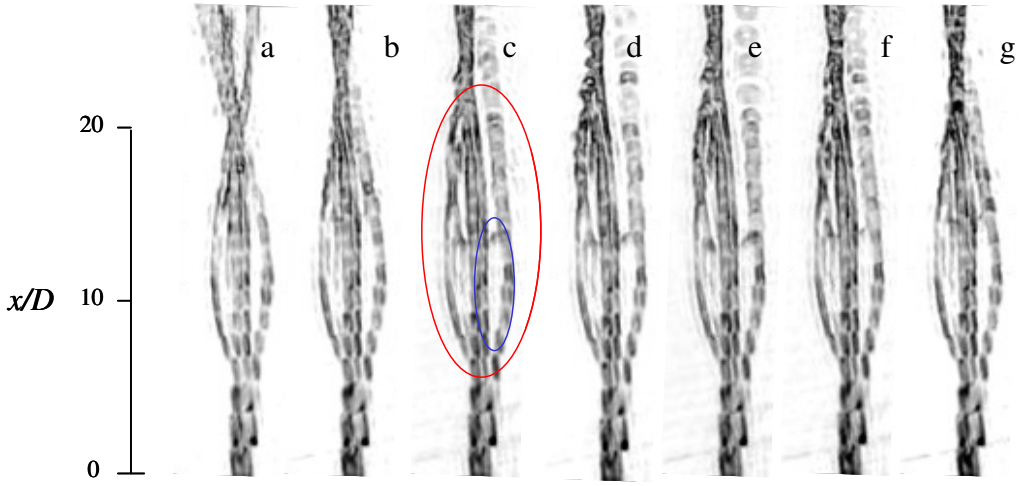

Figure 4.19: Sequence of images showing the opening of the vapor pocket into a hollow cone resulting in branching of the jet column for Re= 500 and P^*=0.065.

The hollow-cone has oscillations may vary with the strength of the "vapor recoil" effect and surface tension both of which fluctuates with the rate of evaporation. When evaporation increases, the "vapor recoil" effect increases and the jet column surface cools. Since the surface liquid is cooler, surface tension is increased and evaporation is decreased with "vapor recoil" resulting in the hollow cone closing. In addition, the rate

of evaporation can fluctuate with local ambient pressure and affect jet column temperature and surface tension.

The location of the hollow-cone is related to the location of the vapor pocket. As a result, the location of the hollow-cone does not vary in time or with P^*. The location of the hollow-cone may vary with *Re*, which has not been studied by previous investigators and the present hollow-cone structures are formed only for *Re*=500.

4.5.3 Steady Branch Formation and Droplet Break up

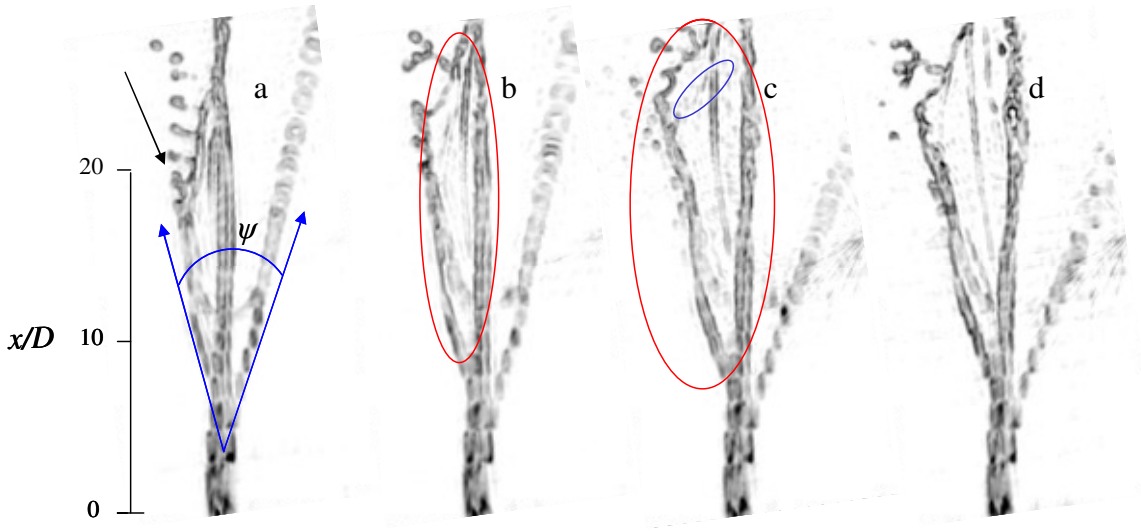

Figure 4.20: Jet branch splay angle increasing with decreased P^* at *Re*= 500: a) P^*=0.072 ψ=29°, b) P^*=0.06 ψ=37°, c) P^*=0.036 ψ=43°, and d) P^*=0.035 ψ=47°.

When $P^* \leq 0.05$, the jet establishes steady branches as shown in Figure 4.20, which is a collection of four images of liquid butane jets. The branches are connected by liquid film as shown in red ovals in Figure 4.20. The jet branches undergo Rayleigh instability and break up while the film in between branches breaks down shedding ligaments. The break up of the far left branch of the jet in Figure 4.20a appears to pull liquid from the film boundaries, causing the film to shed a ligament (indicated by the arrow in Figure

4.20a). The wavy feature (e.g. in the blue oval) on the film-surface of the jet in Figure 4.20c appears to be a surface wave. This hollow-cone structure may be similar to "wings" and film structure produced by 0.1 mm ethanol and ether jets investigated by Kowalewski et al. (1995). The authors described jets that developed "wings" which shed ligaments and had film-like surfaces that developed surface waves.

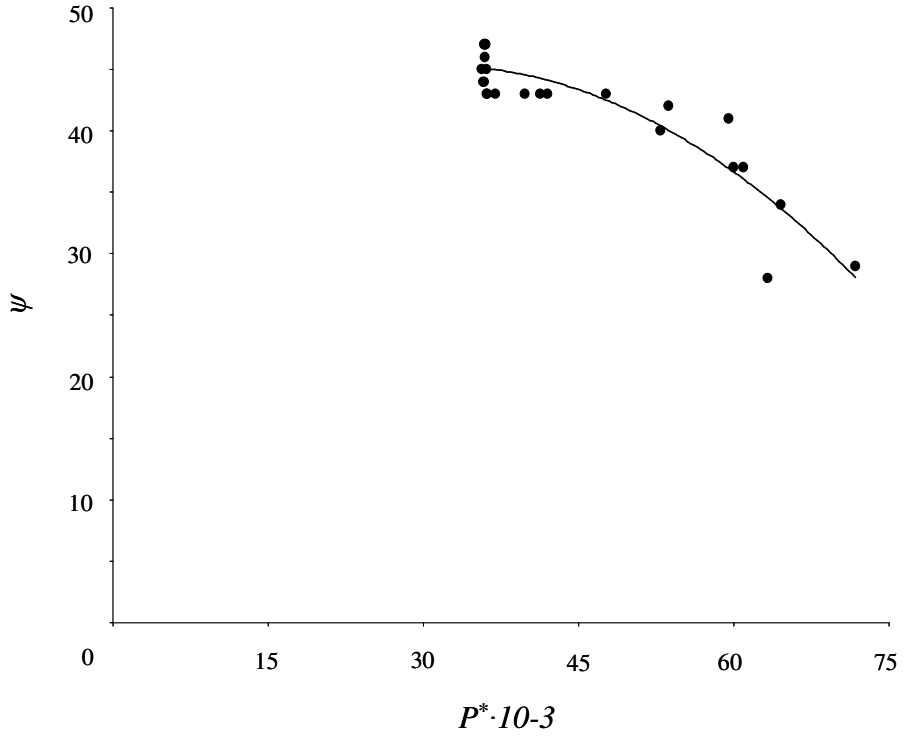

Figure 4.21: Variations of the splay angle (ψ) with P^*, Re=500 and curve $10600(P^*)^2+660(P^*)+35$ (—).

Work reported by earlier investigators does not discuss how the hollow-cone structure varies with P^*. One feature of the hollow-cone structure is the splay angle ψ which is the angle between the two opposite branches of the jet as shown in the Figure 4.20a. The sequence of images in Figure 4.20 shows the jet experiencing greater splay with decreasing P^*. The splay angle of the jet is primarily influenced by the axial force due to the jet momentum and the radial force from surface tension and "vapor recoil." The newly observed effect of P^* in the splaying of the jet has not been investigated and

could be the subject of further theoretical analysis. For the present data, a simple quadratic fit is used as shown in Figure 4.21. These data show that ψ varies as $10600(P^*)^2+660(P^*)+35$. The jet branches gradually splay further with decreasing ambient pressure, finally reaching a point where the splay angle increases with small further decrease in P^* ($P^*\approx 0.035$), indicating the onset of jet flashing. The increases in the splay angle are driven by increased evaporation and vapor recoil inside the hollow-cone structure of the jet as a result of decreased ambient pressure.

4.6 Flashing Instability

Flashing instability is a break up of a liquid jet column into segmented liquid threads or atomized spray as a result of the formation and rupture of vapor bubbles within the jet column. In the present work, this instability occurs for P^*<0.03 and *Re*<1000 or P^*<0.08 and *Re*>1000. There are three manifestations of flashing instability which are discussed here: segmented column, unstable branching, and atomized spray.

Observing the initial bubble formation and growth in the present microscale jets is difficult given the present imaging system. It is not known whether vapor bubbles form within the flow at the nozzle exit or on the internal surfaces of the nozzle, having a roughness of 0.05D therefore may introduce nucleation sites as discussed by Ostrowski (1966).

Although it is difficult to observe vapor bubble formation and growth, it is possible to compute their initial radius and determine their growth rate. As shown by Brown and York (1962), the minimum initial radius, r_o, of an unstable vapor bubble, is given by $r_o = \frac{2\sigma_l}{P_v - P_a}$ where σ_l is the surface tension, P_v is the local vapor pressure, and P_a is the ambient pressure. The minimum initial radius for butane is 83 nm and for propane is 16 nm (evaluating liquid properties at an ambient temperature of 25° C). Brown and York (1962) formed flashing water jets of diameter ranging from 0.5 mm to 2 mm. The authors described the growth of bubbles in those jets in two phases, the initial phase past nucleation where vapor expands the bubble followed by bubble growth that is dominated by heat conduction. The authors claimed that the initial growth phase was the most rapid and that within a few microseconds the bubble radius was 10 times larger than its initial radius. The second phase of growth was referenced to Forster and Zuber (1955) who

showed that $r=r_1+C\cdot t^{0.5}$, where r_1 is the radius after the initial growth, t is time, and C is the growth rate constant. The growth rate constant is given by $C=\left(\frac{C_{p,l}\Delta T}{h_{fg}}\right)\left(\frac{\rho_l}{\rho_g}\right)(\pi\alpha_{th.l})$, where $C_{p,l}$ is the heat capacity of the liquid, ΔT is the degree of superheat, h_{fg} is the latent heat of vaporization, ρ_l is the liquid density, ρ_g is the gas density, and $\alpha_{th.l}$ is the liquid thermal diffusivity. For butane injected into an ambient pressure of 11 kPa, C=0.77 m/s^2. To grow to a radius of 10 μm from 830 nm requires approximately 5 picoseconds. The value does not necessarily contradict the assumption that the initial phase was more rapid, because of the size of the jets of Brown and York (1962). Nevertheless, the results indicate that the time scales and initial length scales for the bubble growth are too small to be resolved by the present imaging system.

4.6.1 Segmented Jet Column and Transition to Spray

The jet column becomes segmented owing to infrequent formation and rupture of vapor bubbles (Figure 4.22a and b). The jet column break up into segments is followed by breaking into a spray when the ruptures occur more frequently (Figure 4.22c and d). Lienhard (1966) illustrated these two forms of flashing break up in a 3.2 mm superheated liquid water jet. He pointed out that if the velocity generated by the bubble explosion (V_e) was greater than the jet velocity (V) then the jet is segmented into liquid threads as shown in Figure 4.22a and b. However, if $V>V_e$ the spray forms.

The persistent transition between the two modes was noted by other investigators and is probably the result of perturbations from the flow within the nozzle (Sections 4.1.1- 4.1.3) which make vapor bubble formation more random. This effect is discussed by Brown and York (1962) when comparing rough and smooth nozzles forming water

jets ranging from 2 mm to 0.5 mm. Nozzle roughness promotes irregular vapor bubble growth and rupture, causing random transitions between segment liquid threads and spray in the present work.

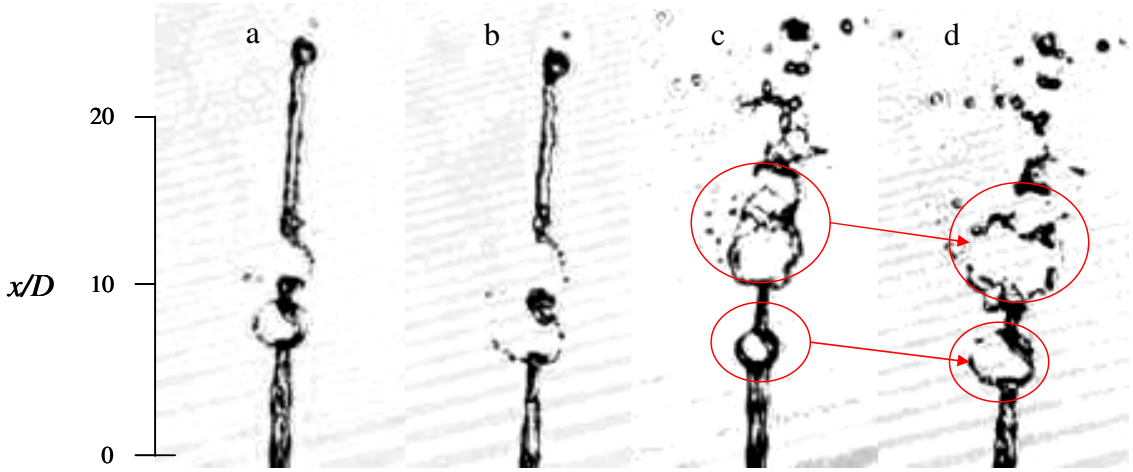

Figure 4.22: Butane jet with flashing instability at Re=1100 and P^*=0.077. Images a) and b) are 1 μs apart and show the segmented column. Images c) and d) are 1 μs and show the jet is on the verge of spray

4.6.2 Unsteady Branching

Flashing jets can also momentarily branch due to vapor bubble formation and rupture, which splays the jet column, an effect that has not been reported in the current literature. The explanation for its transient nature is sought by comparing it to the steady hollow-cone structures observed in the present work. It appears that the films that would form the surfaces of the hollow-cone structure are destroyed by the vapor bubble rupture which prevents enhanced evaporation that would drive the "vapor recoil" effect and maintain a steady branching (shown in the blue oval in Figure 4.23c). In addition, the vapor bubble ruptures severely disturb the formed branches. These disturbances on the branches may give rise to unsteady and nonuniform evaporation from the branches which prevents steady "vapor recoil" or surface tension gradients from maintaining the splay. As a result, this branching is temporary, only lasting a few hundred milliseconds. Figures

4.23a, b, and c show what appears to be the same branched jet and are separated by 300 ms. Finally, the jet reverts to a column jet in Figure 4.23d.

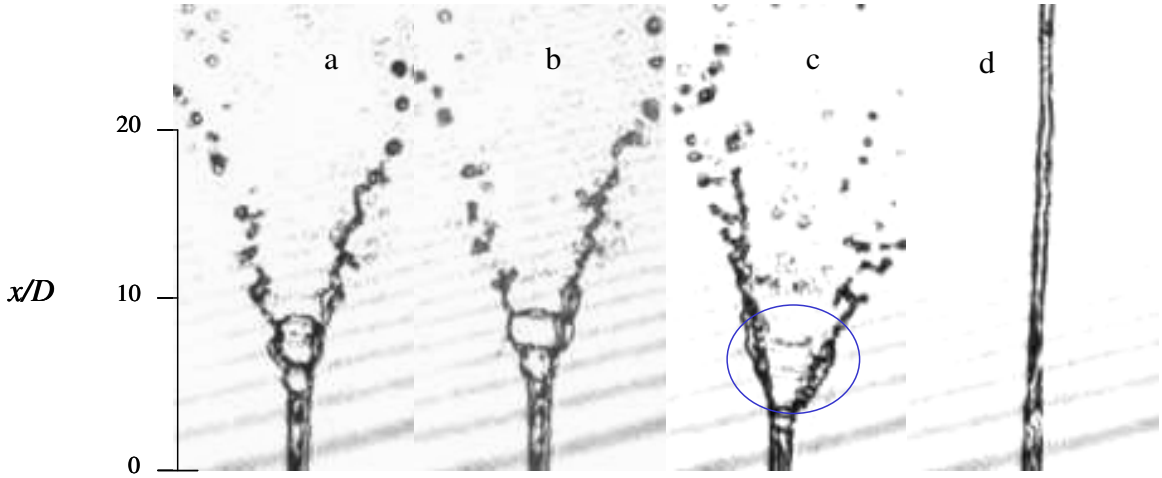

Figure 4.23: Butane jet with vapor bubbles forming and rupturing causing unstable bifurcation *Re*=1100 and P^*=0.077. Images are separated by 300 ms.

4.6.3 Spray Breakdown and Spray Angle

Spraying jets evolve from the orifice as fine droplets that travel downstream and spread radially. The vapor bubbles may be the result of cavitation within the nozzle. For propane jets, the cavitation number ranges from -0.21 to -0.08, which may indicate the occurrence of super-cavitation, but since the nozzle is convergent, there is no evidence to support the presence of flow detachment.

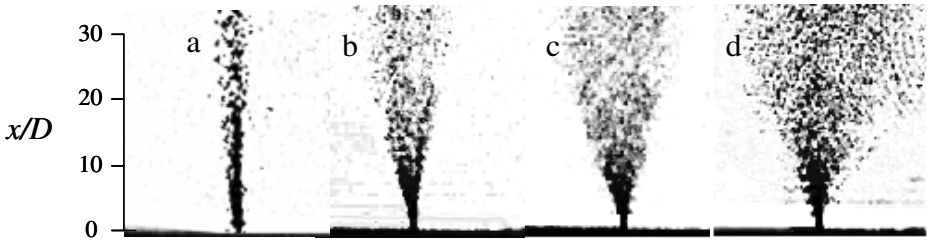

Figure 4.24: Spraying propane jet *Re*=4160 and P^* = 0.103 (a), 0.075 (b), 0.043 (c), and 0.012 (d).

Figure 4.23 shows a propane jet through a range of spray angles as P^* is decreased from left to right. Chaves et al. (1988) described the behavior of the vapor bubbles and

void fractions (cavitation) within the jet as being in mechanical disequilibrium with the ambient pressure. In the present work, as P^* decreases, the rupture of the vapor bubbles become more frequent and more violent. The frequency and energy of the bubble rupture increases with the spray angle. The dependence of the spray angle on P^* is shown in Figure 4.25. A linear fit is selected because of the overall trend of the data and the absence of analytical models for the relationship between P^* and ω. The fit given is for Re=4160, which appears to have the most consistent relationship between P^* and ω. The spray angle follows the fit $-380.4P^*+52$ with R^2=0.95.

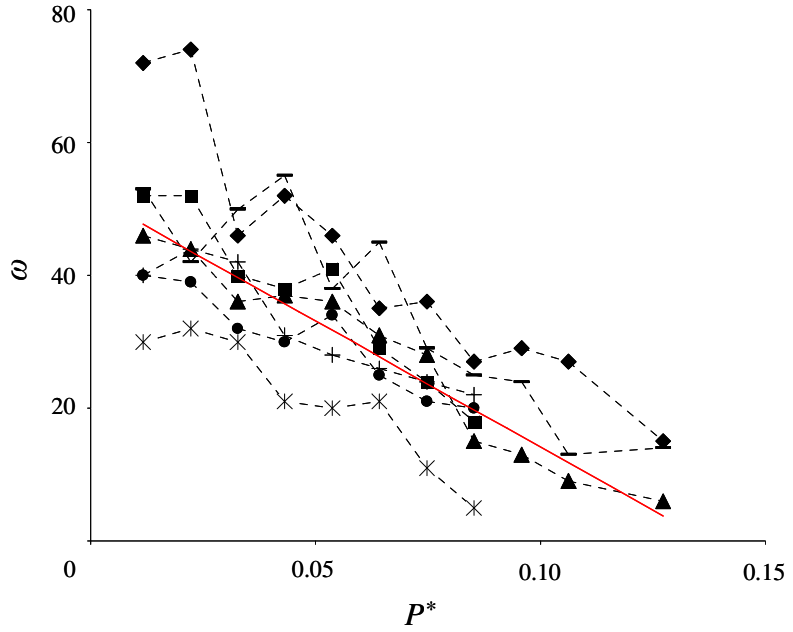

Figure 4.25: Variations of the spray angle (ω) with P^*, Re= 3450(♦), 4060(—), 4160(▲), 4870(■), 5120(∗), 5480(•), and 5480(+) fitted to curve $\omega = -380.4P^*+52$ (—)

The spray angle (ω) of jets at $Re \leq 4060$ tends to be larger than at $Re \geq 4870$ for the same P^* as shown in Figure 4.25. For example, for P^*=0.012, the spray angle at Re=3450 is 70° and at Re=5120 is 28°. There are some irregularities in the data where the Re increases and the spray angle unexpectedly increase (e.g. Re=5120 and Re=5480), but

this is an anomaly probably caused by the present nozzle geometry. The increase in spray angle with decreasing *Re* is expected because of the following relation where $\sin(\omega/2) = V/V_r$, where V is the jet velocity and V_r is the radial velocity. Jet velocity increases with *Re* and radial velocity increases with P^*.

Chapter V

Conclusions

The present work extends the current knowledge of stability and break down of liquid jets to the microscale (O(10 μm)). The behavior of the jet within several instability modes qualitatively agreed with previous observations of instabilities of macroscale liquid jets. Based on the present investigation, a transition map (Figure 5.1) was created to identify the boundaries of these instabilities in terms of the two primary flow parameters P^* and Re.

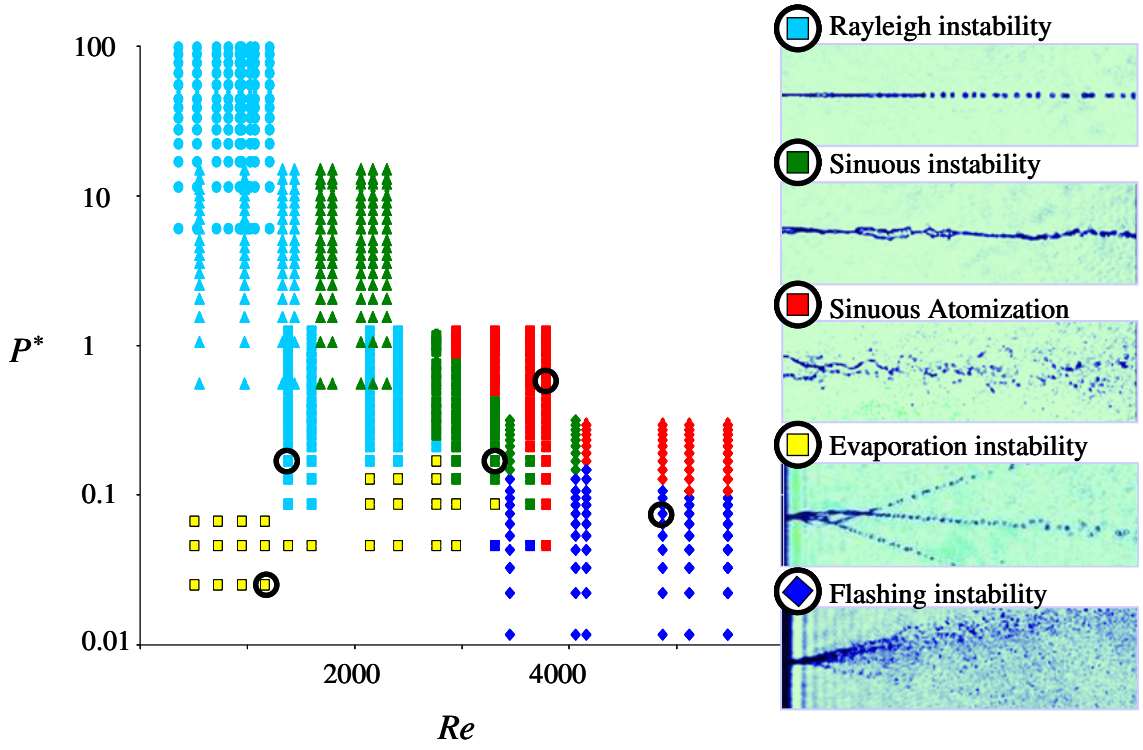

Figure 5.1: Transition map of the column instabilities. Black circles on the transition map show where each image was taken.

Within the domain Re<1500 and P^*>0.1, the evolution of the present microscale liquid jet is dominated by Rayleigh instability. Although downstream of the nozzle exit plane the jet column is somewhat distorted by geometric imperfections of the nozzle, the jet column is restored to a smooth cylindrical section followed by an onset of surface tension driven instability. This instability leads to break up of the jet column to a train of regularly spaced droplets. The present findings show that the break up distance from the exit plane of the jet decreases as P^* decreases. This decrease is apparently caused by evaporation and cooling along the jet column which increases surface tension and therefore amplifies the Rayleigh instability. Above P^*=0.7, evaporative cooling play little role in the break up of the jet because surface tension is not significantly increased. The break up is characterized by the formation of a train of primary droplets that scales with the jet diameter. As a result of the formation of ligaments, satellite droplets having diameters of 0.1D are produced between the primary droplets. These satellite droplets tend to propagate slower than and consequently are consumed by primary droplets. For Re=800, droplet wavelength was approximately 4.5D and produced only primary droplets, as predicted by Rayleigh's linear stability analysis. An increase in the Reynolds number leads to amplification of smaller wavelengths and produces satellite droplets. It is noteworthy that P^* has virtually no effect on the droplet wavelength.

When Re>1500 and P^*>0.1, the liquid jets develop a sinuous instability, which is manifested by a rippled jet column surface and ultimately wiggling of the jet column. Increases in both Re and P^* amplifies the inherent disturbances some of which may be caused by atmospheric interaction as discussed in section 4.1.5. In qualitative agreement with the theoretical model of Weber (1931), the transition to sinuous instability occurs

with a sudden reduction in break up distance from the jet orifice. For the present jet, this transition point occurs at Re=1500. The break up distance decreases as P^* decreases as a result of increased evaporation, which cools the jet, and increases surface tension. Further, increases in Re (Re>2900) and P^* (P^*>1.4) leads to the formation of ligaments that break off the jet column.

Sinuous instability accompanied by atomization is explored for only one case, Re=2950 and P^*=1.93. The evaporation of butane possibly played a role in transition to atomization by increasing the ambient density. The atomized droplets typically formed from strands of liquid that peel off due to jet column wiggling and droplets form by pinching off the ligaments under surface tension forces.

For 0.035<P^*<0.1 and 500<Re<3500, the jet experiences evaporative instabilities which lead to jet column bending, hollow-cone structure formation, and branching of the jet column. Jet bending occurs as a result of the Marangoni effect which is associate with asymmetric evaporation leading to surface tension gradients. Bending butane jets that are produced at this scale without a vapor pocket are steady and maintain a consistent curve as was previously reported by Charwat et al. (1980). As shown in the present work, the butane jet also bends when a vapor pocket is formed, within the jet column. This vapor pocket is sustained by additional pressure from evaporation of liquid from the jet surface referred to as the "vapor recoil" effect by Kowalewski et al. (1993). The vapor pocket transitions from closed to open with increased evaporation. The vapor pocket in the open state appears to be the hollow cone structures that disrupted the jet column similar to those observed by Suzuki et al. (1978). Once the vapor pocket opens, the jet column splits into two or more branch columns. The branched jet columns are joined by a film

and the branches break up into droplets and the film break up into ligaments. The branched state allowed for measurement of the variation of splay angle with P^* and it is found with decreasing P^*, the splay angle increased. This is because the vapor recoil effect increased with reductions in P^*. Eventually, flashing of the liquid jet occurred with further decreases.

When $P^*<0.1$ and $Re>3500$ (region in blue in Figure 5.1), flashing instability causes the jet break up into a spray, segmented column, or unstable branching due to vapor bubble formation and rupture in the jet column. Spray formation and segmented columns effects are already observed and well-studied in flashing macroscale liquid jets. The microscale propane jets formed in the present work were spraying jets which have spray angles that increased with P^*. Increases in *Re* reduces the spray angle, in general, but due to the nozzle geometry, this trend is difficult to see. Microscale liquid butane jets form vapor bubbles that rupture and break the jet column into segments, a phenomenon reported by Lienhard (1966). However due to the small scale of the jet, surface tension forces can sometimes balance violent vapor bubble ruptures to create unsteady bifurcations. This behavior does not appear in any of the literature reviewed, so it is not a feature of traditional macroscale jets.

The present investigation shows agreement in the observed instabilities of macroscale liquid jets to microscale liquid jets. Specifically, the instabilities that show similar break up patterns in the jet column are Rayleigh, sinuous, sinuous with atomization, and flashing instabilities. Microscale liquid jets experiences break up as a result of Rayleigh instability showing both linear (producing only primary droplets) and nonlinear (producing satellite and primary droplets) break up. Amplification of the

perturbations as a result of flow in the nozzle leads to sinuous instability in the jet column and causes decreases in break up distance. These perturbations are shown to increase with ambient pressure causing greater undulations in the jet column and growth of the sinuous instability. Ultimately, the jet experiences sinuous instability with atomization and produces fine droplets (0.1 D) as a result of increases in the ambient pressure. Reducing ambient pressure, the jets experiences evaporative instabilities such as stable jet bending that is dependent on the ambient pressure. Further reductions in ambient pressure, the jet breaks up as a result of flashing instability in two primary forms: segmented jet column and spray jet. The present work shows the spray angle of jets with flashing instability increase with decreasing ambient pressure.

The present research has discovered some new instabilities (e.g. branching) of microscale jets that have not been reported in macroscale jets. Branching liquid jets can be formed by the "vapor recoil" effect or from vapor bubble formation, both of which lead to the separation of the jet column into distinct branches.

The jets in the present work experience branching with the formation of a hollow-cone structure as a result of the evaporative instabilities. For example, at a critical P^*=0.065 for a 10 μm liquid butane jet, the jet oscillates between two states characterized by a vapor pocket trapped within the jet column and a hollow-cone structure with branches. The oscillation between these two states has not been observed in previous investigations. The time scale of the opening and closing of the vapor pocket has yet to be determined and is most likely dependent on surface tension forces, "vapor recoil," and jet velocity which imply that the relevant dimensionless parameters are Ohnesorge number, P^* and Re. Further decreases in P^* leads to the formation of a stable hollow-

cone structure with branches. While the hollow-cone structure was observed by Suzuki et al. (1978) who investigated 0.4 mm superheated water jets, the break up pattern downstream of the hollow-cone was a spray configuration unlike the clearly branched columns observed in the present work. It is shown that the splay of the branches and the appearance of the hollow-cone structure depends on P^*. Suzuki et al. (1978), Charwat et al (1980), and Kowalewski et al. (1993) showed the formation of hollow-cones only for specific values of superheat or ambient pressure, but did not show how the hollow-cone changes with either parameter.

Jets that experience flashing instability branch as a result of vapor bubble formation. This mechanism is differentiated from the trapped vapor pocket structure in the evaporative instability because the rupture of the vapor bubble is a manifestation of the flashing instability and has not been reported by earlier investigators. The rupture of the vapor bubble leads to unsteady branching which may give insights into the mechanisms that give rise to steady branching in jets that undergo evaporative instabilities. More importantly, the lack of film formation may indicate that the hollow-cone structure is crucial to the formation of steady branches, where the rupture of the vapor bubble destroys the film between branches and disturbs the branches. These disturbed branches have distorted surfaces which can experience unsteady and nonuniform evaporation and may prevent the formation of steady surface tension gradients that would maintain the splay in the branches.

References

1. Apostol, T. M. **Linear Algebra**, A Wiley-Interscience Publication, 1997.
2. Arai, M., Shimizu, M., Hiroyasu, H., **"**Similarity between the Breakup Lengths of a High Speed Liquid Jet in Atmospheric and Pressurized Conditions", *Proceedings of the International Conference on Liquid Atomization and Spray Systems*, 61, July 1991.
3. Arai, M., Tabata, M., Hiroyasu, H., and Shimizu, M., **"**Disintegration Process and Spray Characterization of Fuel Jet Injected by a Diesel Nozzle," *Society of Automotive Engineers Technical Paper Series*, **840275**, 1984.
4. Brown, R., and York, L., "Sprays Formed by Flashing Liquid Jets," *AIChE Journal*, **8**, 149-153, 1962.
5. Charwat, A. F., and Russali, R. R., "On the disintegration of Superheated Capillary Jets," *PhysicoChemical Hydrodynamics*, **2**, 55-60, 1981.
6. Chaves, H., Knapp, M., Kubitzek, A., Obermeier, F., Schneider, T., "Experimental Study of Cavitation in the Nozzle hole of Diesel Injectors Using Transparent Nozzles," *SAE Paper*, **950290**, 199-211, 1995.
7. Chaves, H., Kowalewski, T. A., Kurschat, T., Meier, G. E. A., and Müller, E. A., "Similarity in the Behavior of Initially Saturated or Subcooled Liquid Jets Discharging Through a Nozzle," *Chemical Physics*, **126**, 137-143, 1988.
8. Chigier, N. A., "The Physics of Atomization," *ICLASS-91*, 1-15, 1991.
9. Eggers, J., "Dynamics of Liquid Nanojets," *Pys. Rev.*, **89**, 84502-1-4, 2002.
10. Fenn, R. W., and Middleman, M., "Newtonian jet stability: The Role of Air Resistance," *Physics of Fluids*, **15**, 379-383, 1969.
11. Forster, H. K., and Zuber N., "Growth of Vapor Bubbles in Superheated Liquids," *The Journal of Applied Physics*, **25**, 474-478, 1953.
12. Furlani, E. P., "Temporal Instability of Viscous Liquid Microjets with Spatially Varying Surface Tension," *J. Phys. A: Math. Gen.*, **38**, 263–276, 2005.
13. Goedde, E. F. and Yuen, M. C., "Experiments on Liquid Jet Instability," *J. Fluid Mech.*, **40**, 495-511, 1970.
14. Grant, R. P. and Middleman, S., **"**Newtonian Jet Stability," *AIChE Journal*, **12**, 4, 669-678, 1996.
15. Haenlein, A., "Disintegration of a Liquid Jet," *NACA Tech. Memo*, 659, 1932.
16. Hiroyasu, H., "The Breakup of High Speed Jet in a High Pressure Gaseous Atmosphere," *Proceedings of the 2nd International Conference on Liquid Atomization and Spray Systems*, 69-74, 1982.

17. Hiroyasu, H., "Spray Breakup Mechanism from the Hole Type Nozzle and Its Applications", *Atomization and Sprays*, **10**, 511-521, 2000.

18. Hiroyasu, H., Arai, M., Shimizu, M., "Breakup Length of a Liquid Jet and Internal Flow in a Nozzle, *Proc. ICLASS-91*, 123-133, 1991.

19. Holder, D. W., and North, R. J., **Schlieren Methods**, Her Majesy's Stationery Office, 1963.

20. Hoyt, J. W., and Taylor, J. J., "Turbulence Structures in a Water Jet Discharging in Air," *The Physic of Fluids*, **20**, S253-S257, 1977.

21. Ida, M., Nakamura, H., Nakamura, H., Nakamura, H., Ezato, K., Takeuchi, H., "Thermal-hydraulic Characteristics of IFMIF Liquid Lithium Target," *Fusion Engineering and Design*, **63**, 333-342, 2002.

22. Kasyap, T. V., Sivakumar, D., and Raghunandan, B. N., "Breakup of Liquid Jets Emanating from Elliptical Orifices at Low Flow Conditions," *Journal of the International Institutes for Liquid Atomization and Spray Systems,* **18**, 645-668, 2008.

23. Kerst, A. W., Judat, B., Schlünder, E. U., "Flow Regimes of Free Jets and Falling Films at High Ambient Pressure," *Chemical Engineering Science*, **55**, 4189-4208, 2000.

24. Kitamura, Y., and Takahashi, T., "Influence of Nozzle Length on Break Up of a Liquid Jet," *ICLASS-78*, 1-7, 1978.

25. Kowalewski, T. A., Hiller, W. J., and Behnia, M., "An Experimental Study of Evaporating Small Diameter Jets," *Phys. Fluids A*, **5**, 1883-1890, 1993.

26. Kurschat, Th., Chaves, H., and Meier, G. E. A., "Complete Adiabatic Evaporation of Highly Superheated Liquid Jets," *J. Fluid Mech.*, **236**, 43-59, 1992.

27. Lasheras, J. C., and Hopfinger, E. J., "Liquid Jet Instability and Atomization in a Coaxial Gas Stream," *Annu. Rev. Fluid Mech*, **32**, 275-308, 2000.

28. Lienhard, J. H., "An Influence of Superheat Upon the Spray Configurations of Superheated Liquid Jets," *Transactions of ASME*, **88**, 685-687, 1966.

29. Lienhard, J. H., and Day, J. B., "The Break Up of Superheated Liquid Jets," *Transactions of ASME: Journal of Basic Engineering*, **92**, 515-521, 1970.

30. Lin, S. P., **Breakup of Liquid Sheets and Jets**, Cambridge University Press, 2003.

31. Lin, S. P., and Reitz, R. D., "Drop and Spray Formation from a Liquid Jet," *Anuu. Rev. Fluid Mech*, **30**, 85-105, 1998.

32. Mahoney, T. J., and Sterling, M. A., **"**The Breakup Length of Laminar Newtonian Liquid Jets in Air," *Proceedings of the 1st International Conference on Liquid Atomization and Spray Systems*, 9-12, 1978.

33. McCarthy, M. J. and Molloy, N. A., "Review of Stability of Liquid Jets and the Influence of Nozzle Design," *The Chemical Engineering Journal*, **7**,1-20, 1974.

34. Meister, B. J., and Scheele, G. F., "Drop Formation from Cylindrical Jets in Immiscible Liquid Systems," *AlChE Journal*, **15**,700-706, 1969.

35. Middleman , S., and Gavis, J,, "The Expansion and Contraction of Capillary Jets of Newtonian Liquids," *The Physics of Fluids*, **4**, 355-359, 1961.

36. Moseler, M., and Landman, U., "Formation, Stability, and Breakup of Nanojets," *Science*, **289**, 1165-1169, 2000.

37. Nagai, N., Sato, K., and Lee, Ch. W., "Atomization Characteristics of Superheated Liquid Jets," *ICLASS-85*, VB/3/1-10, 1985.

38. Nagaosa, S., Matsui, H., Tokuoka, N., and Sato, G. T., "A Study Disintegration of a Liquid Jet in an Air Flow," *ICLASS-78*, 29-36, 1978.

39. Newman J. A., and Brzustowski, T. A., "Behavior of Liquid Spray at High Pressures", AIAA Paper; **8**, 164-165, 1970.

40. Ostrowski, H. S., "Evaporation and Induced Air Flows in Sprays Produced by Superheated Liquid Jets," PhD Thesis, University of Michigan, 1966.

41. Palmer, H. J., "The Hydrodynamic Stability of Rapidly Evaporating Liquids at Reduced Pressure," *J Fluid Mech,* **75**, 487-511, 1976.

42. Papageorgiou, D.T., "Breakup of liquid jets governed by the Navier-Stokes equations," **Transition, Turbulence and Combustion, Vol. I, Transition**, 225-234, Editors M.Y. Hussaini, T.B. Gatski and T.L. Jackson, 1994.

43. Papageorgiou, D.T., "Analytical Description of the Breakup of Liquid Jets," *J. Fluid Mechanics*, **301**, 109-132, 1995.

44. Phinney, R. E., "Breakup of a Turbulent Liquid Jet in a Low-Pressure Atmosphere," *AIChE Journal*, **21**, 996-1000, 1975.

45. Pimbley, W. T., "Drop Formation from a Liquid Jet: A Linear One-Dimensional Analysis Considered as a Boundary Value Problem," *IBM Journal of Research and Development*, **20**, 148-156, 1976.

46. Plesset, M. S., and Zwick S. A., "Growth of Vapor Bubbles in Superheated Liquids," *The Journal of Applied Physics*, **25**, 493-500, 1953.

47. Rayleigh, J. W. S., "On the Instability of Jets," *Proc. of the Lond. Math. Soc.*, **10**, 4-13, 1879.

48. Rayleigh, J. W. S., **The Theory of Sound**, Macmillan and Company, 1894.

49. Reitz, R. D. and Bracco, F. V. **"**Mechanism of Atomization of a Liquid Jet," *Physics of Fluids*, **25**, 10, 1982.

50. Sallam, K. A., Dai, Z., Faeth, G. M., "Liquid Breakup at the Surface of Turbulent Round Liquid Jets in Still Gases, International Journal Of Multiphase Flow, **28**, 427-449, 2002.

51. Sato, H., and Saito, N., "Non-Linear Wave Propagation and Disintegration of a Circular Liquid Jet," *ICLASS-82*, 19-27, 1982.

52. Savart, F., "Suite du memoire sure le chocd'uneveine liquidelancee contre un plan circulaire," *Ann. Chim. Phys.*, **53**, 337-386, 1833.

53. Settles, G. S., **Schlieren and Shadowgraph Techniques**, Springer-Verlag, 2001.

54. Shin, H., Oschwald, M., Micci, M. M., and Yoon, W., "Influence of Thermodynamic State on Nanojet Breakup," *Nanotechnology*, **16**, 2838-2845, 2005.

55. Sirignano, W. A., and Mehring, C., "Review of Theory of Distortion and Disintegration of Liquid Streams," *Progress In Energy And Combustion Science*, **26**, 609-655, 2000.

56. Smith, S. W. J., and Moss, H., *Proc. Roy. Soc. London A*, **93**, 373, 1916.

57. Sterling, A. M., and Sleicher, C. A., "The Instability of Capillary Jets," *J. Fluid Mech.*, **68**, 3, 477-495, 1975.

58. Suzuki, M., Yamamoto, T., Futagemi, N., and Maeda, S., "Atomization of Superheated Liquid Jet," *ICLAS-78*, 37-43, 1978.

59. Tyler, E., "The Instability of Liquid Jets," *Philosophy Magazine*, **16**, 504-519, 1933.

60. Vieira, M. M., and Simões-Moreira, J. R., "Low Pressure Flashing Mechanism in Iso-Octane Liquid Jets," *J. Fluid Mech.*, **572**, 121-144, 2007.

61. Weber, K., "Zum zerfall eines flüssigkeitsstrahles," *Z. Angew. Math. Mech.*, **11**, 136-154, 1931.

62. Wu, K.-J., Su, C.-C., Steinberger, R. L., Santavicca, D. A., and Bracco, F. V., "Measurements of Atomizing Jets," *Journal of Fluids Engineering: Transactions of ASME*, **105**, 406-413, 1983.

63. Yamaguchi, K., "Micro-machining Using Photo-Polymerization and Metal Jet Deposition," *Proceedings of 1997 Int. Symposium on Micromechatronics and Human Science*, 33-40, 1997.